Title
Consequences of systematic model drift in DYNAMO MJO hindcasts with SP-CAM and CAM5

Journal
Journal of Advances in Modeling Earth Systems, 7(3)

ISSN
1942-2466

Authors
Hannah, Walter M
Maloney, Eric D
Pritchard, Michael S

Publication Date
2015-09-01

DOI
10.1002/2014ms000423

Peer reviewed

AGU PUBLICATIONS

Journal of Advances in Modeling Earth Systems

RESEARCH ARTICLE
10.1002/2014MS000423

Special Section:
The 2011-12 Indian Ocean Field Campaign: Atmospheric-Oceanic Processes and MJO Initiation

Consequences of systematic model drift in DYNAMO MJO hindcasts with SP-CAM and CAM5

Walter M. Hannah[1,2], Eric D. Maloney[3], and Michael S. Pritchard[4]

[1]Department of Atmospheric Science, University of Miami, Miami, Florida, USA, [2]Now at Department of Marine, Earth, and Atmospheric Sciences, North Carolina State University, Raleigh, North Carolina, USA, [3]Department of Atmospheric Science, Colorado State University, Fort Collins, Colorado, USA, [4]Department of Earth System Science, University of California Irvine, Irvine, California, USA

Key Points:
- SP-CAM better reproduces DYNAMO MJO events compared to CAM5
- Systematic drift in SP-CAM projects onto the RMM and impacts RMM skill scores
- Systematic drift in SP-CAM enhances synoptic eddies that affect column moisture

Correspondence to:
W. M. Hannah,
walter@hannahlab.org

Citation:
Hannah, W. M., E. D. Maloney, and M. S. Pritchard (2015), Consequences of systematic model drift in DYNAMO MJO hindcasts with SP-CAM and CAM5, *J. Adv. Model. Earth Syst.*, *7*, 1051–1074, doi:10.1002/2014MS000423.

Received 31 DEC 2014
Accepted 12 JUN 2015
Accepted article online 16 JUN 2015
Published online 14 JUL 2015

Abstract Hindcast simulations of MJO events during the dynamics of the MJO (DYNAMO) field campaign are conducted with two models, one with conventional parameterization (CAM5) and a comparable model that utilizes superparameterization (SP-CAM). SP-CAM is shown to produce a qualitatively better reproduction of the fluctuations of precipitation and low-level zonal wind associated with the first two DYNAMO MJO events compared to CAM5. Interestingly, skill metrics using the real-time multivariate MJO index (RMM) suggest the opposite conclusion that CAM5 has more skill than SP-CAM. This inconsistency can be explained by a systematic increase of RMM amplitude with lead time, which results from a drift of the large-scale wind field in SP-CAM that projects strongly onto the RMM index. CAM5 hindcasts exhibit a contraction of the moisture distribution, in which extreme wet and dry conditions become less frequent with lead time. SP-CAM hindcasts better reproduce the observed moisture distribution, but also have stronger drift patterns of moisture budget terms, such as an increase in drying by meridional advection in SP-CAM. This advection tendency in SP-CAM appears to be associated with enhanced off-equatorial synoptic eddy activity with lead time. Systematic drift moisture tendencies in SP-CAM are of similar magnitude to intraseasonal moisture tendencies, and therefore are important for understanding MJO prediction skill.

1. Introduction

Weather has intrinsic limits of predictability [*Lorenz*, 1968], but the practical shortcomings of observation networks and numerical prediction methods are often the biggest factor limiting forecast skill. Convectively, coupled phenomena are especially prone to errors because of the uncertainties surrounding the treatment of convection in large-scale models. Luckily, these errors on the mesoscale and smaller tend to saturate within the first few days of a forecast, allowing large-scale patterns to have longer predictability [*Zhang et al.*, 2007]. For example, convectively coupled equatorial waves can maintain their amplitude and, in principle, can be predicted out to 2 weeks, in spite of the fact that moist convection largely influences the dynamics [*Straub et al.*, 2006; *Mapes et al.*, 2008].

A potential source of enhanced prediction skill of variability on subseasonal time scales is the Madden-Julian Oscillation (MJO) [*Zhang*, 2013], which is characterized by alternating intraseasonal periods of enhanced convection and wind in the Tropical Indian and West Pacific Oceans regions [*Madden and Julian*, 1972; *Zhang*, 2005]. The MJO can interact with many weather phenomena, such as tropical cyclones [*Vitart*, 2009; *Vitart et al.*, 2010], the Asian and Australian monsoons [*Hendon and Liebmann*, 1990; *Joseph et al.*, 2008], African easterly waves [*Matthews*, 2004; *Alaka and Maloney*, 2012], extratropical weather [*Cassou*, 2008; *Marshall et al.*, 2010; *Vitart and Molteni*, 2010], and ENSO [*Shi et al.*, 2010]. Because of its long time scale, quasiperiodic nature, and far-reaching effects, the MJO offers the potential of improving weather prediction beyond the typical range of weather forecasts [*Zhang*, 2013].

It has long been recognized that most weather and climate models cannot reproduce robust MJO variability [*Slingo et al.*, 1996; *Lin et al.*, 2006; *Kim et al.*, 2009, *D. Kim et al.*, 2014]. This problem is often attributed to issues with the treatment of moist convection [*Tokioka et al.*, 1988; *Maloney and Hartmann*, 2001; *Lin et al.*, 2008b; *Hannah and Maloney*, 2011, 2014; *Benedict et al.*, 2014], but a detailed understanding of this problem is lacking. In addition to the lack of a robust MJO in most free-running global models, MJO prediction skill is also lacking in operational forecast systems [*Ling et al.*, 2014]. The inherent predictability of the MJO has

been estimated to be around 30–40 days [*Waliser et al*., 2003; *Ding et al*., 2010; *H.-M. Kim et al*., 2014; *Neena et al*., 2014]. However, most studies find the actual MJO prediction skill to be about 10–20 days for individual models [*Vitart et al*., 2007; *Seo et al*., 2009; *Rashid et al*., 2010; *Vitart et al*., 2010; *Klingaman and Woolnough*, 2014] and 10–30 days when an ensemble approach is used [*Neena et al*., 2014]. While this range is beyond the ∼10 day limit of typical forecasts, there is room for improvement in forecast systems, as well as in the methods used to assess forecast skill [*Ling et al*., 2014].

Hannah and Maloney [2014] analyzed hindcast experiments of the MJO events that occurred during the dynamics of the MJO (DYNAMO) international field campaign, which took place in the Indian Ocean during the winter of 2011–2012 to study the initiation of the MJO [*Yoneyama et al*., 2013; *Johnson and Ciesielski*, 2013]. The experiments used a common approach of increasing the entrainment rate for deep convection, which tends to strengthen the MJO signal in a model [*Maloney and Hartmann*, 2001; *Bechtold et al*., 2008; *Hannah and Maloney*, 2011]. However, their results suggest that this method actually produces a better MJO for the wrong reason. Specifically, increasing convective entrainment allows divergent circulations to become unrealistically efficient at building up column moist static energy. This produced an unrealistic trade-off whereby too strong import by vertical moist static energy advection compensated for other model deficiencies, such as weak cloud-radiative feedbacks, and explained why the stronger entrainment parameter helped improve the MJO.

A more recent approach to treating convection in global models, known as "superparameterization," is able to produce a robust MJO with attractively fewer assumptions about how moist convection behaves [*Khairoutdinov et al*., 2005; *Benedict and Randall*, 2009; *Thayer-Calder and Randall*, 2009; *Zhu et al*., 2009; *Andersen and Kuang*, 2012; *Pritchard and Bretherton*, 2014]. Superparameterization works by representing the effects of unresolved moist convection and turbulence processes with an embedded higher-resolution model, often referred to as a cloud-resolving model (CRM), that is specialized for the unresolved scales of convection [*Khairoutdinov and Randall*, 2001; *Jung and Arakawa*, 2005]. The downside of this approach is that it can substantially increase computational expense [*Randall et al*., 2003], although there are strategies to compensate for this while maintaining MJO fidelity [*Pritchard et al*., 2014].

Kim et al. [2009] found the superparameterized NCAR Community Atmosphere Model (SP-CAM) to have the most realistic composite MJO simulation out of eight state-of-the-art, uncoupled global models. A recent study has shown in 20 day hindcasts of specific MJO events during the Year of Tropical Convection (YOTC) that SP-CAM is among the best of 15 AGCMs in 15–20 day outgoing longwave radiation (OLR) forecast skill [*Klingaman et al*., 2015]. An explanation for these successes is not clear. Some have suggested that SP-CAM's success is due to the ability to delay deep convection until the troposphere can be sufficiently moistened [*Zhu et al*., 2009]. A delay in deep convection should allow more vigorous convection after the environment has been sufficiently primed, unlike models that allow deep convection in dry environments [*Grabowski and Moncrieff*, 2004; *Bechtold et al*., 2008; *Thayer-Calder and Randall*, 2009]. Radiative processes have also been implicated to play an important role in the maintenance and propagation of the MJO [*Andersen and Kuang*, 2012; *Chikira*, 2014]. SP-CAM calculates radiative tendencies on the CRM grid, which produces realistic cloud-radiative feedbacks, and so we expect this model to produce a more realistic MJO in this respect.

The representation of the MJO in SP-CAM is not without some deficiencies. Generally, the convective intensity of the MJO is too strong, which may be due to differences in the model's mean state, and unrealistic interactions between deep convection and the boundary layer [*Benedict and Randall*, 2009]. *Klingaman et al*. [2015] found that despite its good OLR forecast skill, SP-CAM is among the poorest performing third of 15 AGCMs in RMM and wind 15–20 day forecast skill for YOTC MJO events. Some have suggested that the SP-CAM may also have an unrealistically intense wind-evaporation feedback stemming from the periodic boundaries in the embedded CRM [*Luo and Stephens*, 2006]. Some of the deficiencies noted above may be improved through coupling SP-CAM to an ocean model [*Stan et al*., 2010; *Benedict and Randall*, 2011; *DeMott et al*., 2014].

When initialized with an observed state, models are known to systematically drift away from initial conditions toward a state consistent with their internal physics [*Judd et al*., 2008]. However, little work has been done to characterize the drift of superparameterized models. Systematic errors in hindcasts with the conventionally parameterized CAM tend to resemble model biases in long-term simulations [*Ma et al*., 2013].

Most of the hindcast error that results from systematic drift of an atmospheric model is evident by day 2 of a simulation and generally becomes saturated by day 5 [*Xie et al*., 2012]. These systematic errors are mostly associated with moist processes, but can also be associated with dry, balanced dynamics [*Jung*, 2005]. Systematic drift also tends to be different depending on the region and time of year [*Kang et al*., 2004; *Huang et al*., 2007; *Vitart et al*., 2007]. Many methods can be utilized to reduce such errors, such as multimodel ensembles that cancel out systematic errors [*Pavan and Doblas-Reyes*, 2000], or statistical methods [*Feddersen et al*., 1999]. It may be tempting to correct systematic errors, but their existence can shed light on model deficiencies that can be addressed to produce a more physically consistent solution [*Phillips et al*., 2004; *Ma et al*., 2013].

In light of the advantages of superparameterization, the current paper compares hindcast simulations of DYNAMO MJO events from a conventionally parameterized model (CAM5) that was analyzed by *Hannah and Maloney* [2014] to its superparameterized counterpart (SP-CAM). The analysis focuses on the consequences of systematic model drift in both models, including the implications for assessing model MJO skill using metrics commonly employed in the community [*Rashid et al*., 2010; *Klingaman et al*., 2015]. Section 2 outlines the methods and model configurations. Section 3 details differences between the models and characterizes the effect of systematic model errors on skill scores. Effects of drift on the budget of column moisture are considered in section 4. Conclusions are discussed in section 5.

2. Methodology

2.1. Hindcast Setup

Simulations are conducted with the Super-Parameterized Community Atmosphere Model version 5 (SP-CAM), which is the atmospheric component of the NCAR Community Earth System Model version 1.1 (CESM) [*Neale et al*., 2010]. The development of SP-CAM is a bit unconventional, occurring across several institutions, which has complicated the version history. The version used in this study was obtained from the NCAR subversion server, but is currently not available to the public. This issue will likely be resolved as superparameterized models becomes more widely available, but to ensure repeatability of our results we are willing to share our code and data with any interested party. The embedded cloud-resolving model used to simulate subgrid-scale convection in SP-CAM is based on the System for Atmospheric Modeling (SAM) [*Khairoutdinov and Randall*, 2003], including updates to modern versions of CAM and upgrades to SAM microphysics and radiative transfer capabilities by *Wang et al*. [2011]. The domain of the embedded cloud-resolving model (CRM) is a two-dimensional "curtain," with 32 columns and 28 vertical levels corresponding to the lowest 28 levels in CAM. A Newzed with Arakawa C staggering, and a third-order Adams-Bashforth time stepping scheme with variable time stepping to maintain linear stability. A single-moment bulk microphysics scheme is used, with five species of hydrometeors, including cloud water, rain, cloud ice, snow, graupel, and hail. All simulations employ a finite volume dynamical core, 30 vertical levels and $0.9^\circ \times 1.25^\circ$ horizontal resolution. Note that this horizontal resolution of SP-CAM is generally higher than that used in the literature at this time.

Hindcasts with the conventional CAM5, which employs the deep convection scheme of *Zhang and Mcfarlane* [1995], are also conducted for comparison. To be consistent with *Hannah and Maloney* [2014] we use the default deep convective entrainment rate of 1.0 km^{-1}. CAM5 contains a moist boundary layer scheme based on *Bretherton and Park* [2009], the prognostic two-moment bulk cloud microphysics scheme of *Morrison and Gettelman* [2008], and the shallow convection scheme of *Park and Bretherton* [2009]. No cloud parameterizations are needed in SP-CAM, since the embedded CRM takes the place of all of these parameterizations.

Hindcast initial conditions were created from ECMWF operational analysis at 00z every 5 days from 1 October 2011 to 15 December 2011. While a higher density of hindcast initializations (daily) could have been useful for constraining statistical sampling significance, we prefer a sparse hindcast initialization methodology since this alleviates concerns about whether the hindcasts are truly independent on the temporal scales relevant to the MJO [*Vitart et al*., 2007]. Furthermore, the high cost of running SP-CAM at $\sim 1^\circ$ resolution limited our ability to substantially increase the number of simulations. Each simulation was integrated for 10 days with output every 6 h. The initialization of hindcasts with SP-CAM raises the question of whether it is necessary for the embedded CRM to be "spun-up" prior to the initialization time. There is currently no

published study that addresses this question. The third author of this study has experimented with nudging methods that allow subgrid convection to develop prior to hindcast initialization. These experiments have not yielded any notable difference in event-level MJO forecast skill when compared to a "cold start" method. Similar intrinsic predictability experiments confirm that including versus excluding CRM-scale state information at hindcast initialization has no effect on MJO forecast skill in multievent composites in SP-CAM. Based on this experience, and since a nudging approach adds complexity, and thus we have opted to use a "cold start" method for this study.

Hindcast skill is estimated using the Real-time Multivariate MJO index (RMM) [*Wheeler and Hendon*, 2004] following *Rashid et al*. [2010], *Lin et al*. [2008a], and *Gottschalck et al*. [2010] to estimate a bivariate correlation (COR) and root mean square error (RMSE) of the hindcast RMM given by

$$COR(\tau)=\frac{\sum_{t=1}^{N}\left[a_1(t)b_1(t,\tau)+a_2(t)b_2(t,\tau)\right]}{\sqrt{\sum_{t=1}^{N}\left[a_1^2(t)+a_2^2(t)\right]}\sqrt{\sum_{t=1}^{N}\left[b_1^2(t,\tau)+b_2^2(t,\tau)\right]}}, \tag{1}$$

$$RMSE(\tau)=\sqrt{\frac{1}{N}\sum_{t=1}^{N}\left\{\left[a_1(t)-b_1(t,\tau)\right]^2+\left[a_2(t)-b_2(t,\tau)\right]^2\right\}}, \tag{2}$$

where $a_{1,2}(t)$ is the verification RMM and $b_{1,2}(t,\tau)$ is the respective projection of the forecast onto the observed RMM patterns for time t and lead time τ. To first order, *COR* is generally insensitive to amplitude errors and so should be considered as a measure of RMM phase skill in the hindcast, whereas *RMSE* is sensitive to both phase and amplitude errors. Since both indices are normalized by their standard deviations, an *RMSE* of 2.0 or above indicates that the two indices are no longer correlated, and therefore the model can be viewed as having no skill beyond this threshold. Similarly, we use a threshold minimum of 0.5 for *COR* to indicate when a hindcast has no skill, consistent with previous studies [*Rashid et al*., 2010]. Note that we retain interannual variability in our RMM calculation.

The RMM projections for each hindcast are obtained following previous studies [*Lin et al*., 2008a; *Rashid et al*., 2010; *Gottschalck et al*., 2010], with the exception that we retain interannual variability, since we are working with a short hindcast period. This exception does not affect the interpretation of skill scores since the verification RMM data also retain interannual variability. To be consistent with previous studies, the RMM projections are estimated using the NCEP-NCAR reanalysis [*Kanamitsu et al*., 2002] zonal wind at 200 and 850 hPa, and NOAA-interpolated OLR [*Liebmann and Smith*, 1996]. The procedure for obtaining hindcast RMM projections is as follows:

1. Hindcast anomalies are calculated by subtracting the 31 year climatological mean and seasonal cycle of NCEP and NOAA OLR data over the period 1980–2010.
2. The hindcast data are latitudinally averaged over 15°S–15°N.
3. Each field is divided by a normalization factor from *Wheeler and Hendon* [2004]:
   a. 1.81 m s^{-1} for 850 hPa zonal wind.
   b. 4.81 m s^{-1} for 200 hPa zonal wind.
   c. 15.1 W m^{-2} for OLR.
4. Hindcast data are then projected onto the observed EOF patterns.
5. Finally, the projection coefficients are divided by the observed principal component standard deviations from *Wheeler and Hendon* [2004] based on 1979–2001 values.

2.2. Validation Data

To validate the SP-CAM and CAM5 hindcasts, we use the European Centre for Medium-Range Weather Forecasts (ECMWF) operational analysis that was used to create the hindcast initial conditions, as well as the Tropical Rainfall Measuring Mission (TRMM) 3B42 3 hourly merged satellite rainfall product. Both data sets have a high spatial resolution of 0.25°, which is interpolated to match the model grid.

2.3. Subsetting Method

Several following analyses in this study will utilize a subset of the hindcast and observational data that will be grouped by lead times of either 00–04 or 05–09 days. The hindcast initializations are separated by 5 days, and so the 00–04 and 05–09 day lead times can be concatenated to form continuous data sets. The observation-based validation data can be similarly subsetted to match the days covered by the hindcast

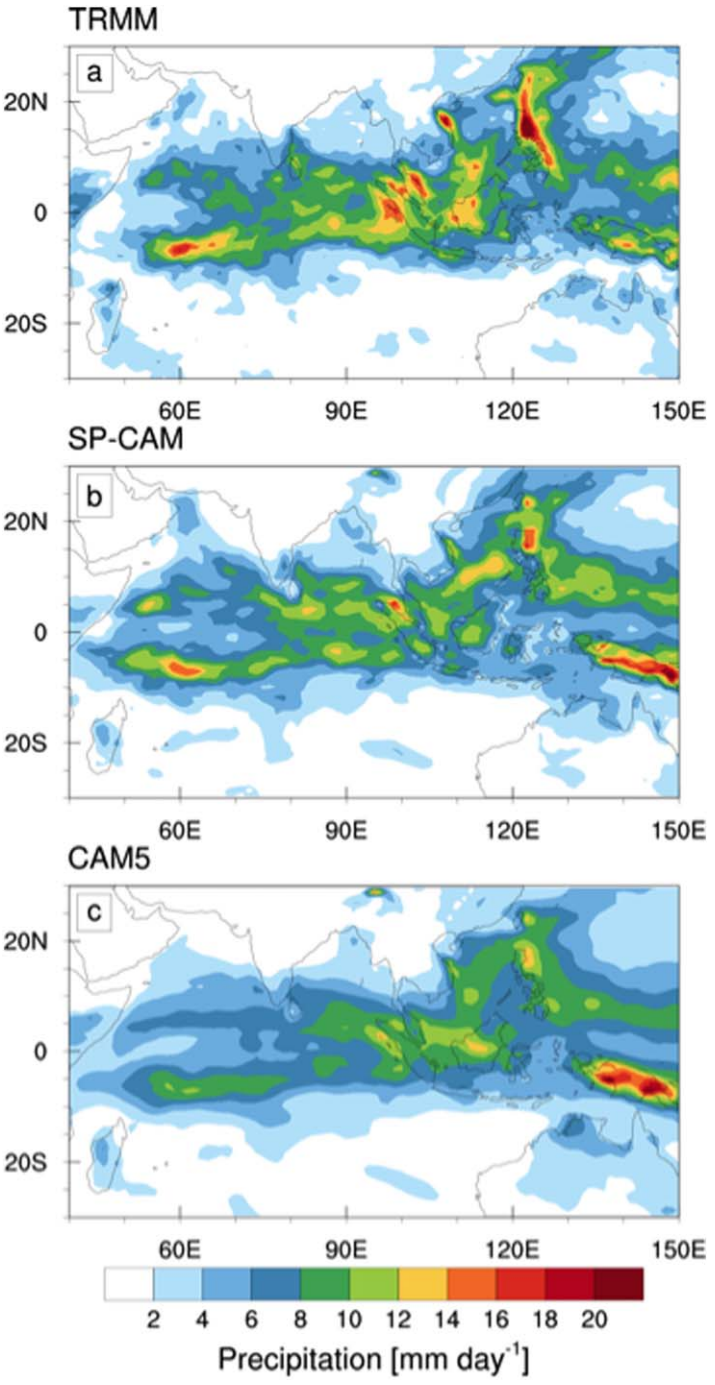

Figure 1. Mean precipitation for all data with a lead time of 00–04 days.

data in either case. This allows us to easily compare the first and second halves of the hindcast data, in order to characterize how the quality of the hindcast degrades with lead time.

3. Hindcast Drift and RMM Skill Metrics

3.1. Hindcast Comparison

Our initial goal is to determine how each model performs in the DYNAMO hindcast simulations, since convection is treated very differently in each model. Maps of precipitation averaged over data with 00–04 day lead times are shown in Figure 1 for TRMM, SP-CAM, and CAM5. The simulations exhibit some region-specific precipitation biases, but generally resemble TRMM observations. SP-CAM is slightly more realistic than CAM5, with areas of intense precipitation over the Indian Ocean. The models also share some differences relative to TRMM, such as too much precipitation over Papua New Guinea and too little precipitation near the Philippines (Figures 1b and 1c).

To get a sense of how well the hindcasts capture the DYNAMO MJO events, Hovmöller diagrams of equatorial averaged precipitation for 00–04 day leads are shown in Figure 2. The data in Figure 2 have been temporally smoothed with two passes of a 1-2-1 filter to bring out MJO-scale variability. TRMM shows clearly defined periods of enhanced precipitation that make up the October and November DYNAMO events (Figure 2a). SP-CAM also shows periods of enhanced and suppressed precipitation that agree well with TRMM data, but are slightly less coherent (Figure 2b). The MJO events are less prominent in CAM5 (Figure 2c), but periods of enhanced and suppressed precipitation still occur at the correct longitudes and times. Precipitation in CAM5 is generally weaker than SP-CAM or TRMM, consistent with the mean precipitation in Figure 1c.

At 05–09 day lead times the MJO precipitation signal is somewhat degraded in both models (Figure 3). SP-CAM still maintains clear periods of enhanced and suppressed precipitation, although the convective envelope is less coherent than in TRMM data (Figure 3b). Degradation of the convective signal is more dramatic

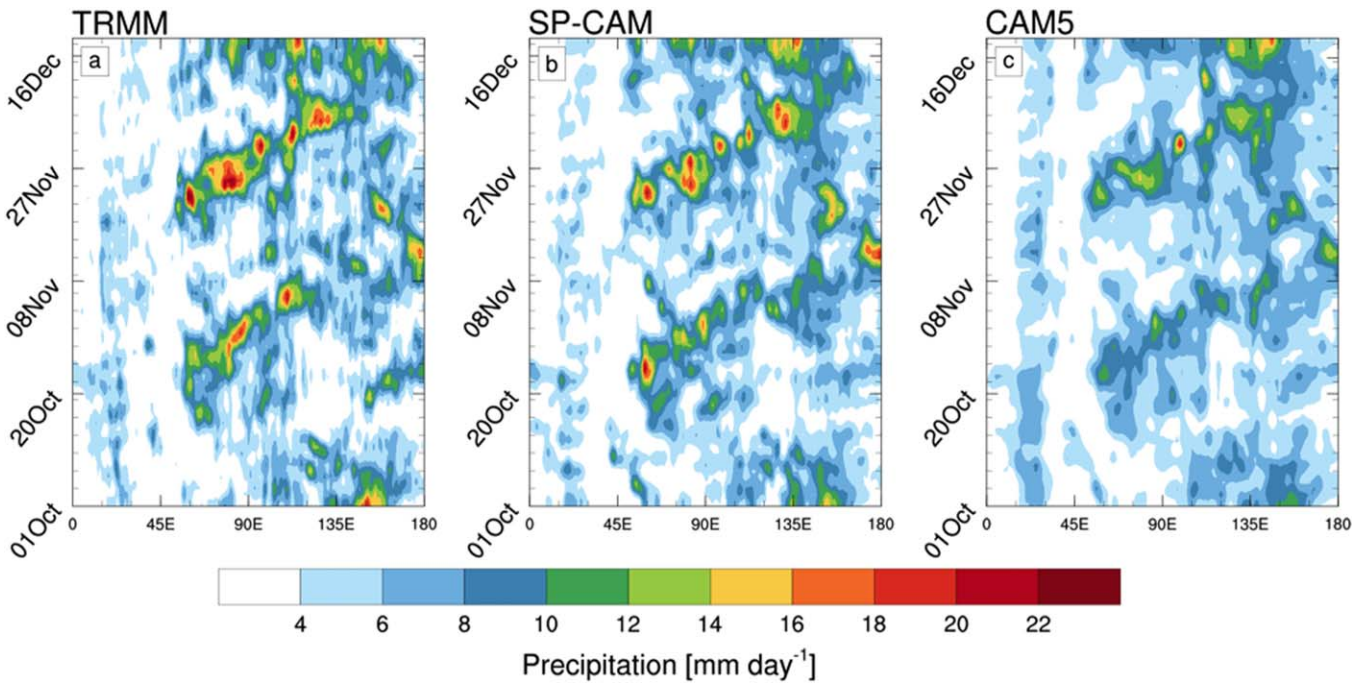

Figure 2. Hovmöller diagram of equatorial precipitation averaged from 15°S to 15°N for 00–04 day lead times.

in CAM5 at 05–09 day leads (Figure 3c). Overall, we conclude that SP-CAM hindcasts have a more robust representation of the MJO convective signal during DYNAMO when compared to the conventional CAM5.

Figure 4 shows Hovmoller plots of 850 hPa zonal wind for ECMWF, SP-CAM, and CAM5 at 00–04 day leads. Both models slightly overestimate low-level zonal wind anomalies (Figure 4b), evidenced by higher standard deviations of 3.3 m s^{-1} for SP-CAM and 3.0 m s^{-1} for CAM5 versus 2.7 m s^{-1} for ECMWF data. A similar overestimation is found for upper level wind anomalies (not shown). At 05–09 day leads the zonal wind

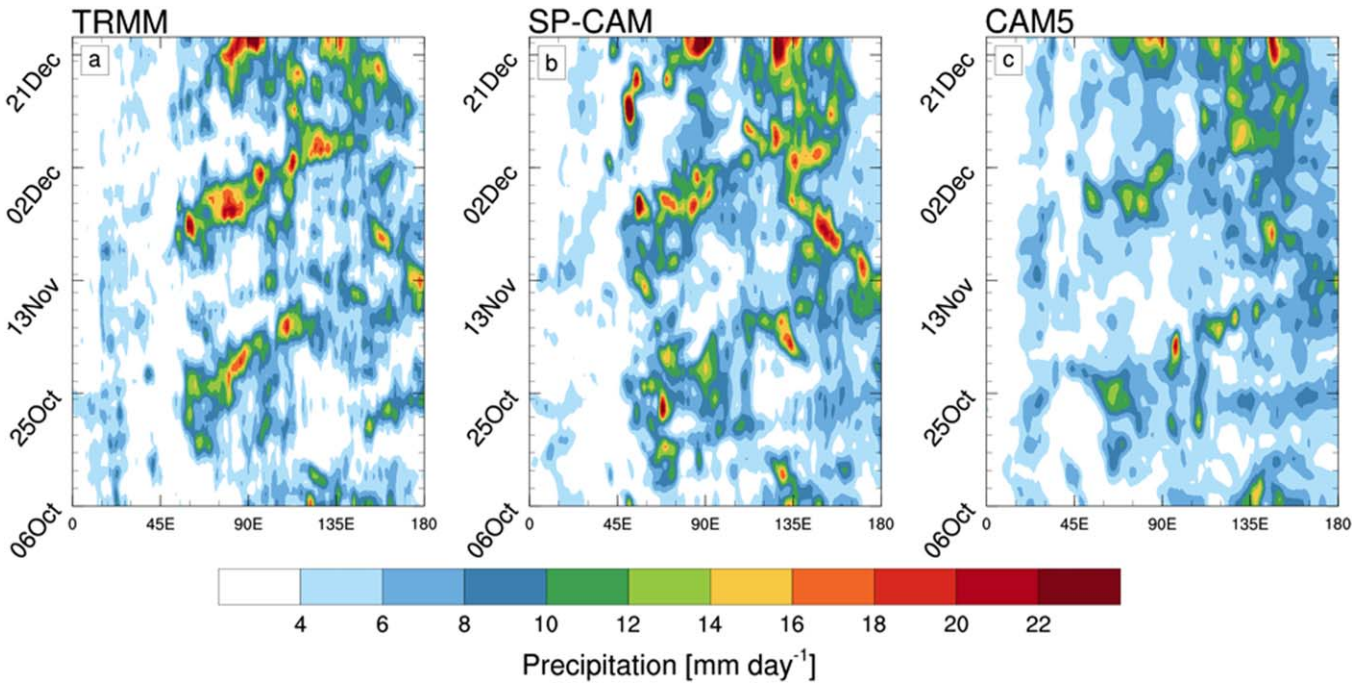

Figure 3. Hovmöller diagram of equatorial precipitation averaged from 15°S to 15°N for 05–09 day lead times.

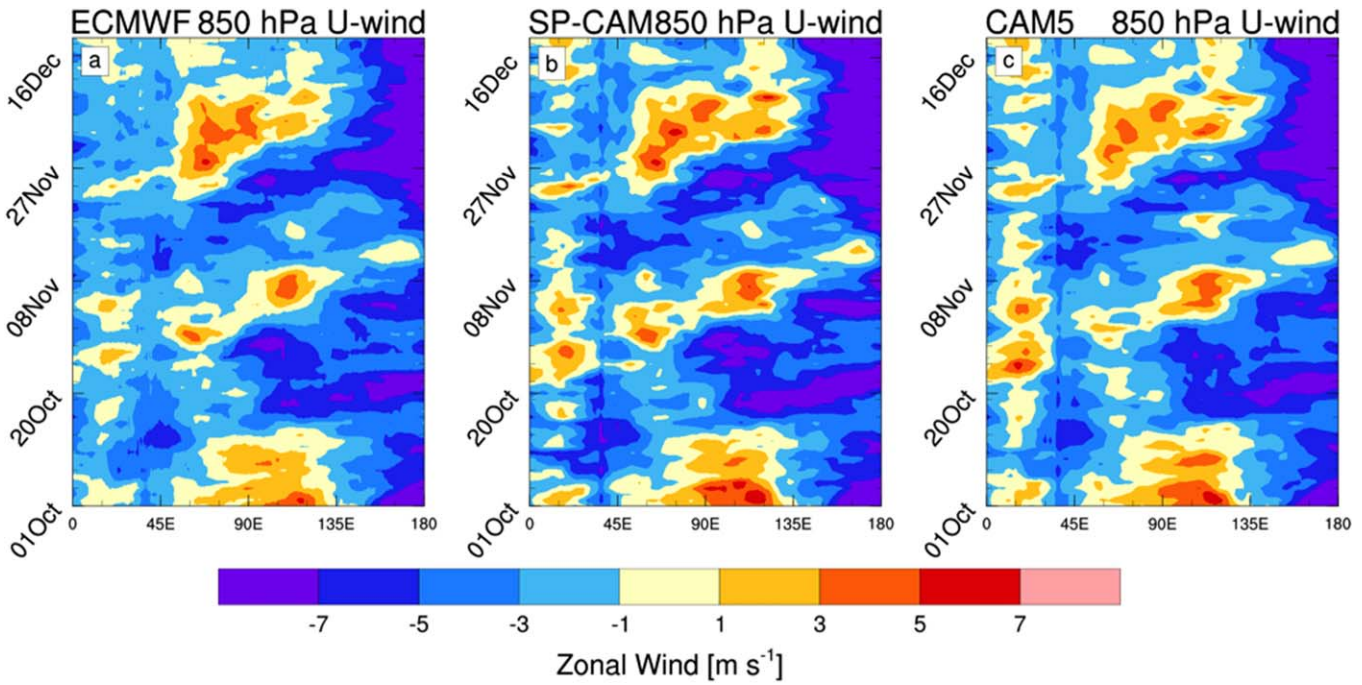

Figure 4. Hovmöller diagram of equatorial 850 hPa zonal wind averaged from 15°S to 15°N for 00–04 day lead times.

signal in both models has become less coherent, especially for CAM5 (Figure 5). Interestingly, the magnitude of the zonal wind generally becomes stronger at later lead times in SP-CAM. As we will show, this property of SP-CAM can strongly affect the projection onto the RMM index.

3.2. RMM Skill Metrics

The COR and RMSE skill scores are shown in Figure 6. Note that the COR and RMSE scores on the first day are not 1.0 and 0.0, as might be expected. This is partly because the model is initialized at 00Z and exhibits an adjustment during the first 24 h, but also because we initialize from ECMWF data, but use NCEP data for the RMM projection, following previous studies [*Gottschalck et al*., 2010]. The COR metric (higher value is better) indicates a slightly better skill in SP-CAM than CAM5 (Figure 6a). On the other hand, the RMSE metric (lower value is better) suggests that SP-CAM has less skill than CAM5 in predicting future MJO evolution, which may at first glance seem inconsistent with Figures 2–5. This discrepancy suggests a large amplitude error in SP-CAM. The RMM index mostly emphasizes wind fields rather than OLR [*Straub*, 2013], so the high RMSE is likely related to the overestimation of the wind signal (Figures 4 and 5).

To better understand the amplitude error in SP-CAM, it is useful to first deconstruct the time series of RMM amplitude and phase for each hindcast simulation relative to the observed RMM index (Figure 7). The amplitude and phase of the RMM index are calculated from the RMM components (RMM_1 and RMM_2) as follows:

$$AMP = \sqrt{RMM_1^2 + RMM_2^2}, \tag{3}$$

$$PHS = \arctan\left(\frac{RMM_2}{RMM_1}\right) \tag{4}$$

A systematic overamplification of the RMM projection in SP-CAM is evident in Figure 7a, whereas CAM5 hindcasts more closely follow the observed RMM (Figure 7b). Both models do an adequate job of reproducing the RMM phase (Figures 7c and 7d). This confirms that our conclusion from the RMM skill metrics was correct in that an amplitude error exists in SP-CAM. The amplitude problem in SP-CAM is the opposite of the overly weak MJO amplitude that exists in many models [*Kim et al*., 2009, *D. Kim et al*., 2014; *Neena et al*., 2014; *H.-M. Kim et al*., 2014].

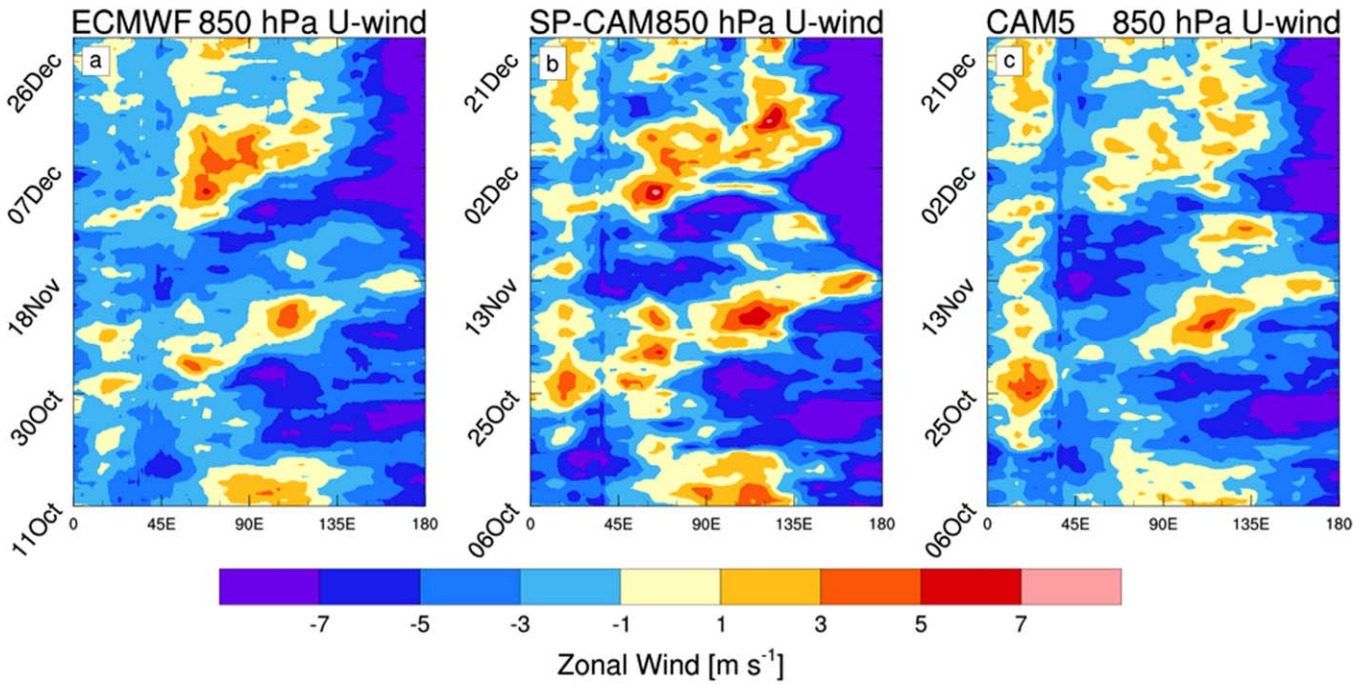

Figure 5. Hovmöller diagram of equatorial 850 hPa zonal wind averaged from 15°S to 15°N for 05–09 day lead times.

Figure 8 reveals a striking drift signal in SP-CAM hindcasts. Time series of individual SP-CAM RMM components (Figures 8a and 8c) reveal a systematic tendency for SP-CAM hindcasts to have an increasingly strong projection onto positive RMM_1 and negative RMM_2. This is not to say that errors are not evident at other phases, but a selective amplification of positive RMM_1 and negative RMM_2 appears to be robust across all the SP-CAM hindcasts, regardless of initial MJO phase. In contrast, CAM5 does not show any systematic errors that grow with lead time (Figures 8b and 8d). In CAM5 there are both positively and negatively trending biases of the RMM components at different initial MJO phases. In other words, a systematic drift in the wind field occurs in SP-CAM hindcasts that does not occur in the standard CAM5.

Note that it is not valid to interpret RMM_1 and RMM_2 separately from a physical standpoint because they both describe a single mode of variability. Here we are discussing the projection of a model solution that is physical inconsistent with the real world onto the RMM index and the influence on MJO hindcast skill. Thus, in this case, it is useful to consider the RMM components separately to help explain how and why model

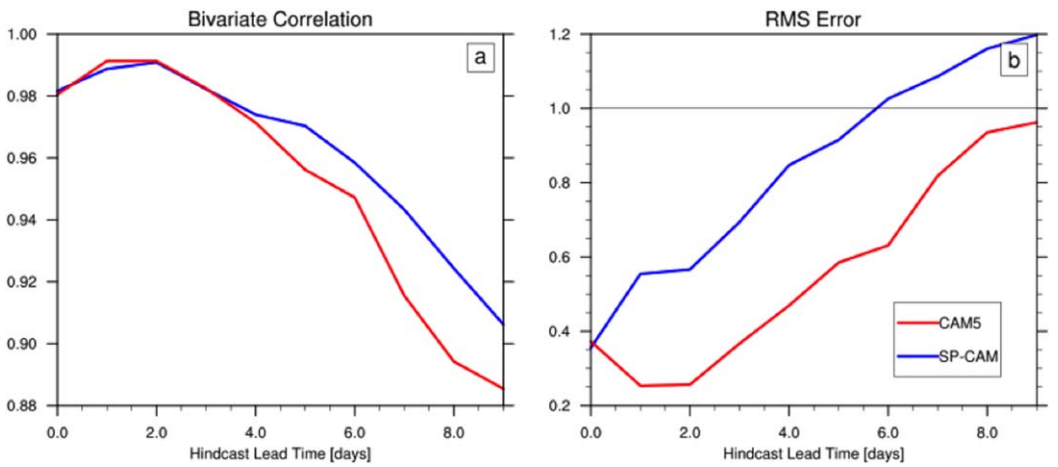

Figure 6. (left) COR and (right) RMSE RMM skill scores as a function of lead time in days for SP-CAM (blue) and CAM5 (red). The thin black line denotes a threshold of no MJO predictive skill (see text).

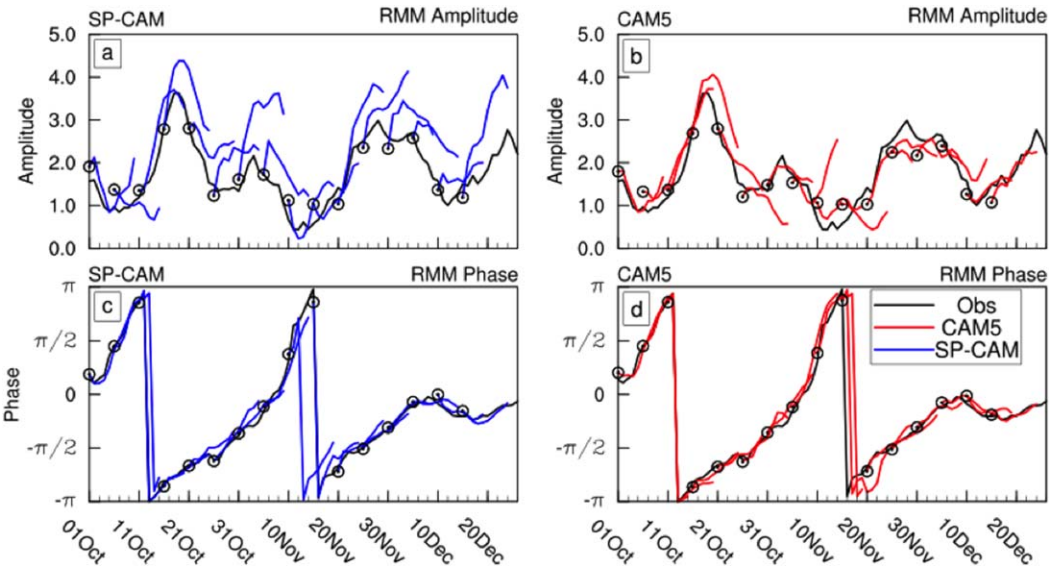

Figure 7. (a) Time series of RMM amplitude, (b) RMM_1, (c) RMM phase, and (d) RMM_2 from observations (black) and individual (left) SP-CAM (blue) and (right) CAM5 (red) hindcast projections.

drift with a geographic preference impacts the RMM skill scores (Figure 6). In light of our conclusion, the amplitude problem identified initially by the RMM skill metrics may have little to with the model's intrinsic ability to produce a coherent representation of the DYNAMO MJO events. To better understand whether this is the case, we need to quantify the impact of the models' drift pattern and verify that it projects onto positive RMM_1 and negative RMM_2.

3.3. Impacts of Model Drift on the RMM

In order to quantify model drift, we need to first isolate the drift signal. Model drift is a systematic evolution of the model state, independent of perturbations in the initial conditions. To isolate the drift of a variable, we first locate all data that fall on a given lead time. We then average these data to get a four-dimensional data set that is a function of lead time and the three spatial dimensions. The purpose of this averaging is to remove the "weather" and bring out the signal of the intrinsic model drift that occurs systematically over

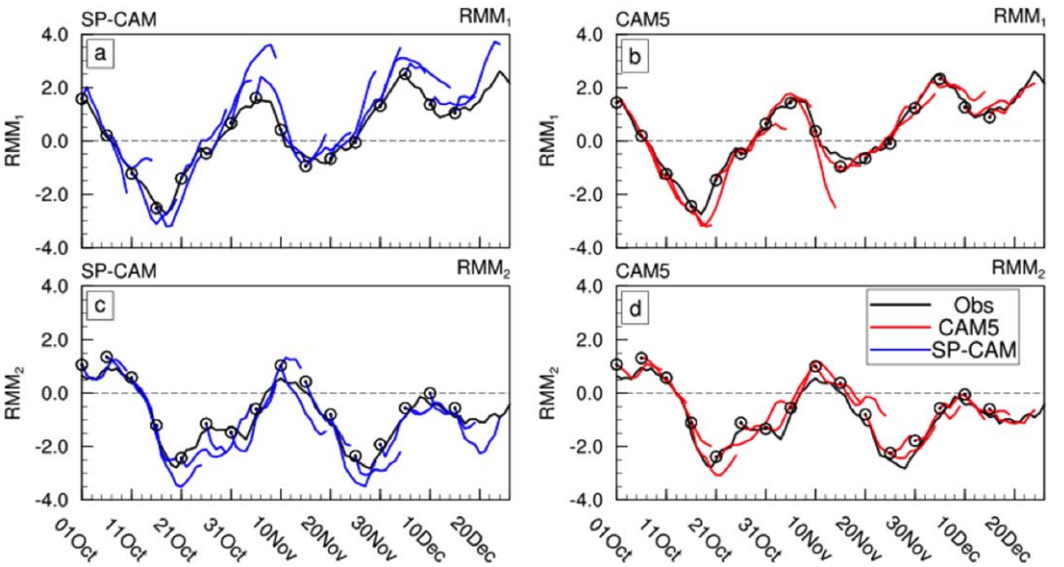

Figure 8. Time series of RMM index components, (top) RMM_1 and (bottom) RMM_2, for (left) SP-CAM and (right) CAM5.

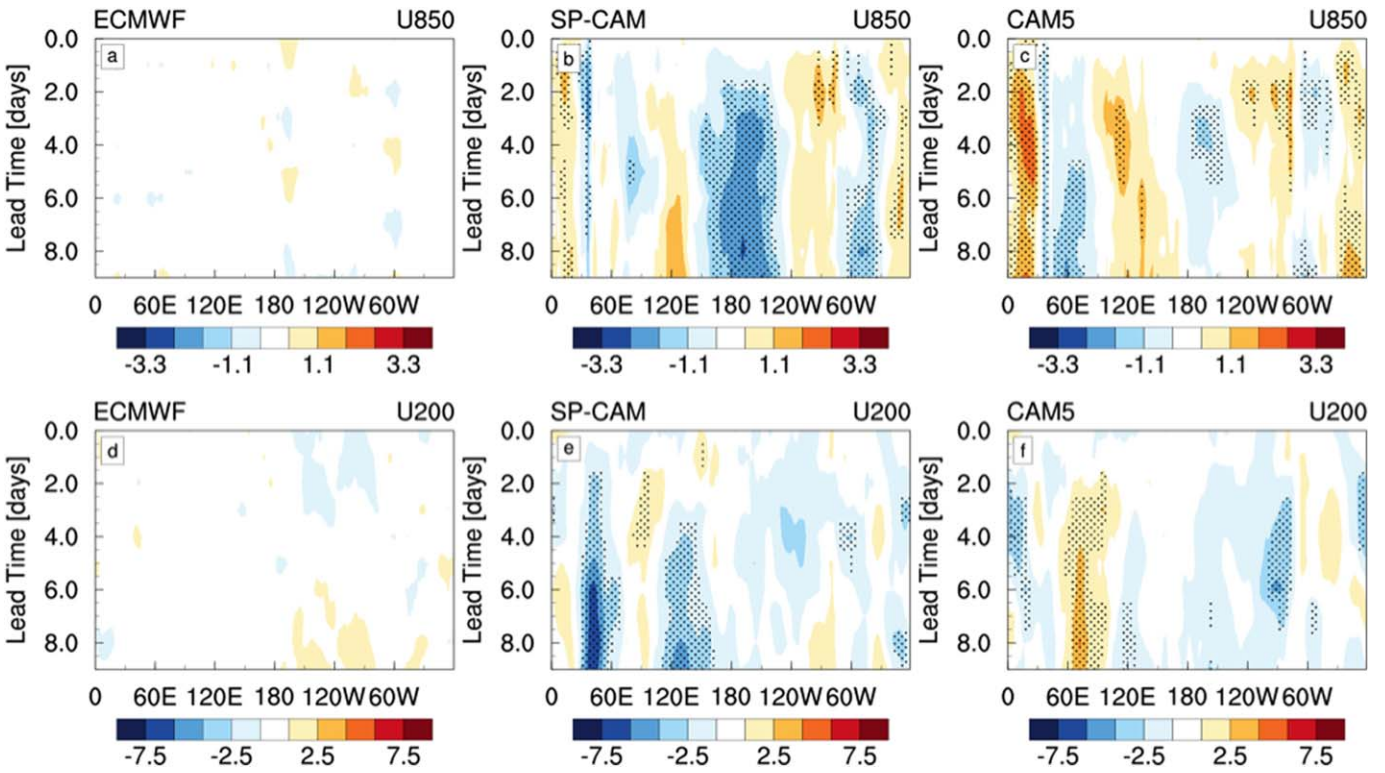

Figure 9. Hovmöller diagrams of the systematic drift over the DYNAMO period as a function of time since hindcast initialization (see text) in the wind fields used in the RMM index in ECMWF, SP-CAM, and CAM5. Contour units are m s^{-1}. Stippling indicates where the drift signal is significantly different than zero at the 95% cofidence level. Data were equatorial averaged from 15°S to 15°N, consistent with the RMM index.

the course of each hindcast. As an illustrative example, the first time of this new data set would be the average of the first time output of all hindcasts for a given model (ex. 00Z on 1 October, 5 October, 10 October, etc.). The "drift" of the observational data is similarly calculated by selecting the days that correspond to each lead time of the hindcast data.

At this point, we could subtract the value at the initial hindcast state, but this can be misleading when a variable has a large error at the time of initialization and becomes closer to the observed state at a later time. Quantities related to moist convection, such as precipitation, tend to exhibit this behavior (not shown). A better method is to subtract the temporal mean of the verification data (i.e., ECMWF analysis) from the hindcast drift signal at all spatial points. In this sense the drift can be considered a component of the total hindcast error. Comparison of drift patterns to average hindcast error patterns (i.e., not based on the RMM) reveals that drift patterns do not necessarily resemble error patterns, and are generally smaller in magnitude (not shown).

Note that the drift obtained from the hindcasts in this study is limited in scope, and may not fully describe the intrinsic model drift, since drift can have a seasonal dependence. A more thorough method of characterizing the drift tendencies of a model would be to create hindcasts for each day of the year over several decades so that any seasonal evolution of the systematic model drift could be accounted for. Indeed, this is the strategy used as a best practice to analyze the effect of convection parameterization changes on intrinsic MJO skill as distinct from model drift in the ECMWF model development process [e.g., *Vitart et al.*, 2007]. Unfortunately, SP-CAM is so computationally expensive that this alternate method is too burdensome, and thus outside the scope of the present study.

To characterize the effect of drift on the RMM index, equatorially averaged Hovmöller plots are shown in Figure 9 for 850 and 200 hPa zonal wind (U850; U200). Results from ECMWF analysis are included to confirm there is no drift in the analysis, except for a slight hint of the seasonal cycle in the upper level wind over the East Pacific (Figures 9a and 9d). In the simulations, upper and lower level wind display a drift pattern with a rich longitudinal structure. SP-CAM develops a strong low-level easterly bias around 180°E–120°W (Figure 9b).

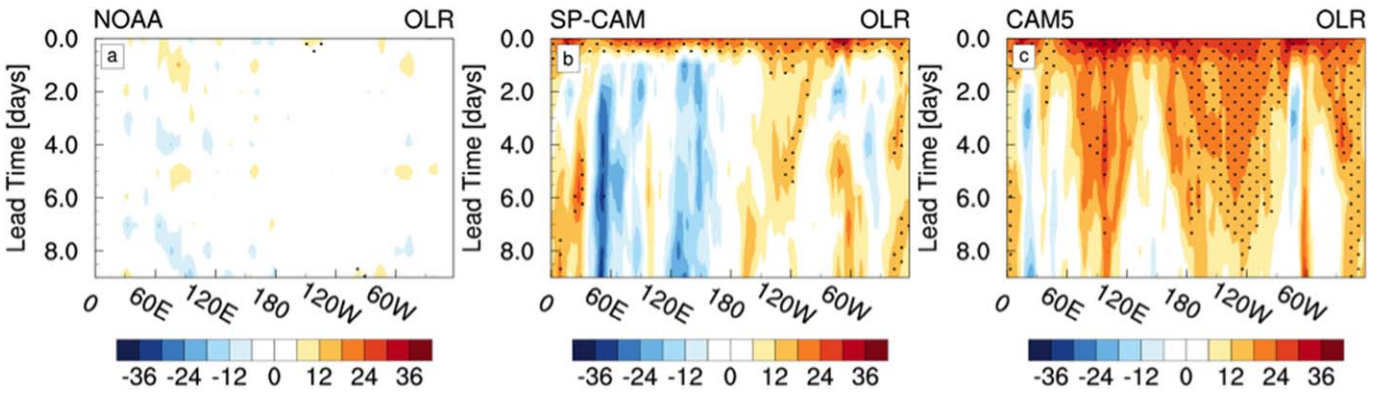

Figure 10. Hovmöller diagrams of the systematic drift, similar to Figure 9, except for OLR with units of W m^{-2}. NOAA OLR is used as the reference to isolate the model drift signal.

There is a weak signal of a similar low-level easterly bias in CAM5 (Figure 9c). Upper level wind drift in SP-CAM shows a prominent easterly bias (Figure 9e). CAM5 also has a mostly easterly upper level zonal wind drift, as well as a westerly bias in the central Indian Ocean. The drift pattern of zonally averaged meridional wind also shows a similar diverse spatial structure, but does not indicate a robust shift of the ITCZ (not shown).

Although OLR has a small impact on the RMM [*Straub*, 2013], it is interesting to consider how it evolves in the simulations. To isolate the OLR drift we use NOAA OLR as a reference, since this is used in the RMM (Figure 10). The OLR drift in SP-CAM is reminiscent of a zonal wavenumber one pattern, with a stronger reduction of OLR (i.e., enhanced cloudiness) in the Indian Ocean and West Pacific Oceans (60°E–180°E). This pattern appears likely to project well onto the RMM spatial patterns, which also have a similar wavenumber 1 pattern. The OLR drift in CAM5 also shows a reduction in OLR with lead time, but the drift begins with a larger positive bias and is more gradual than the OLR drift tin SP-CAM. Both models show higher OLR (i.e., suppressed convection) at day 0. This might be related to the spin-up of the embedded CRM in SP-CAM. Parameterized convection in CAM5 does not require such spin-up, but the ambient cloud water and ice used in radiative calculations is initially absent, and therefore some time is required to adjust these fields to reasonable values.

Now that we have a method for isolating the systematic hindcast drift as an anomaly from the ECMWF data, we can further quantify the full impact of the drift signal on the RMM index by projecting the equatorially averaged drift data (15°S–15°N) at each lead time onto the RMM spatial structures defined by *Wheeler and Hendon* [2004]. The projection of the drift signal is calculated in a similar manner to the RMM projections used for the skill score calculations, except in this case we have removed the mean of the ECMWF "drift" data, rather than the climatological mean and seasonal cycle. Figure 11 shows the SP-CAM RMM drift projection on the RMM components as well as the individual projections of U200, U850, and OLR. The drift projections confirm the selective amplification of positive RMM_1 and negative RMM_2 suggested in Figure 8. During days 0–6, U200 compensates the positive RMM_1 bias, but later becomes positive (Figure 11a). Although wind dominates the RMM index, Figure 11 suggests that OLR also contributes substantially to the RMM amplification problem. The biggest offender to both RMM_1 and RMM_2 in SP-CAM is U850, contributing the strongest drift signal to the RMM bias. Similar plots for CAM5 show the model drift weakly contributing a negative RMM_1 and positive RMM_2 (Figure 12). Therefore, we can conclude that model drift in CAM5 is less of a concern for interpreting the RMM skill scores. On the other hand, the SP-CAM nicely reproduces the convective signal of the DYNAMO MJO events, but the model drift induces a large bias in the RMM projections, and obscures the RMM RMSE metric. The significant mean state drift in SP-CAM may reflect the fact that it is an experimental prototype tool that has not been substantially tuned in its mean state, unlike the standard CAM and older versions of SP-CAM [*Pritchard and Bretherton*, 2014].

Even though an exhaustive characterization of model drift is outside the scope of this study, we can naively estimate the effect of the drift shown here on the RMM skill scores. The solid lines in Figure 13 show the result of estimating the RMM skill metrics after removing the systematic drift that was used to produce Figures 9 and 10. Although the drift was less prominent in CAM5, removing it has improved the phase error so that SP-CAM and CAM5 have comparable COR values over the 10 day hindcast (Figure 13a). However, the COR change is relatively small, and thus does not appear to be strongly influenced by the systematic drift.

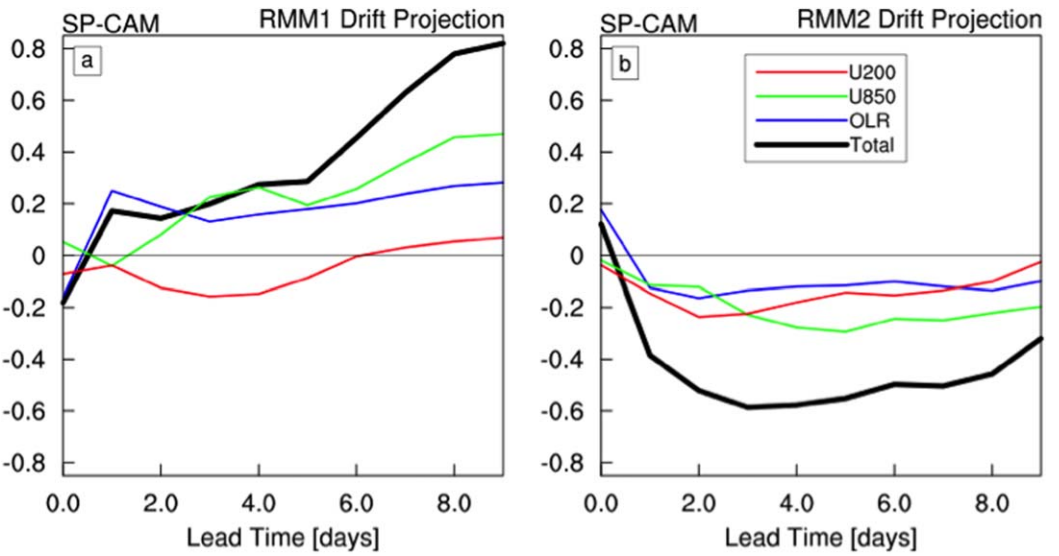

Figure 11. Projection of the isolated drift pattern in Figures 9 and 10 onto the RMM spatial structures (see text) as a function of lead time for SP-CAM. The total projection (thick black) is broken into three components of the projection from OLR (blue), U850 (green), and U200 (red).

RMSE is noticeably reduced for SP-CAM when the drift is removed (Figure 13b), but it is still significantly higher than CAM5. This difference may be due to the stronger variability of lower tropospheric wind in SP-CAM (Figure 5), since stronger anomalies of both signs would not be a consequence of model drift. A detailed explanation of why the drift-corrected RMM skill scores change as shown in Figure 13 is complicated by the nonlinearity of the skill score calculations in (1) and (2). Additionally, we feel a larger hindcast ensemble is needed to estimate the significance of the differences in Figure 13.

4. Effects of Hindcast Drift on Column Moisture

The drift patterns highlighted in the previous analysis are interesting from an operational viewpoint, because they give us insight into how the RMM skill scores can be misleading if a model has large drift. From a more scientific perspective, the question naturally arises as to how model drift might affect the fundamental dynamics of the MJO. The RMM is an empirical tool for identifying the MJO that cannot tell us

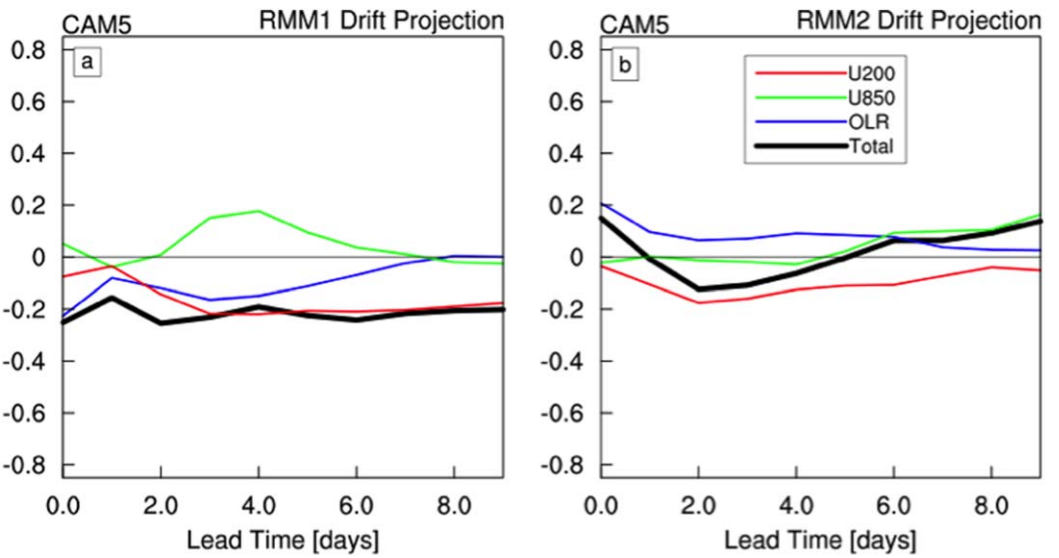

Figure 12. Projection of the isolated drift pattern, similar to Figure 11, except for CAM5.

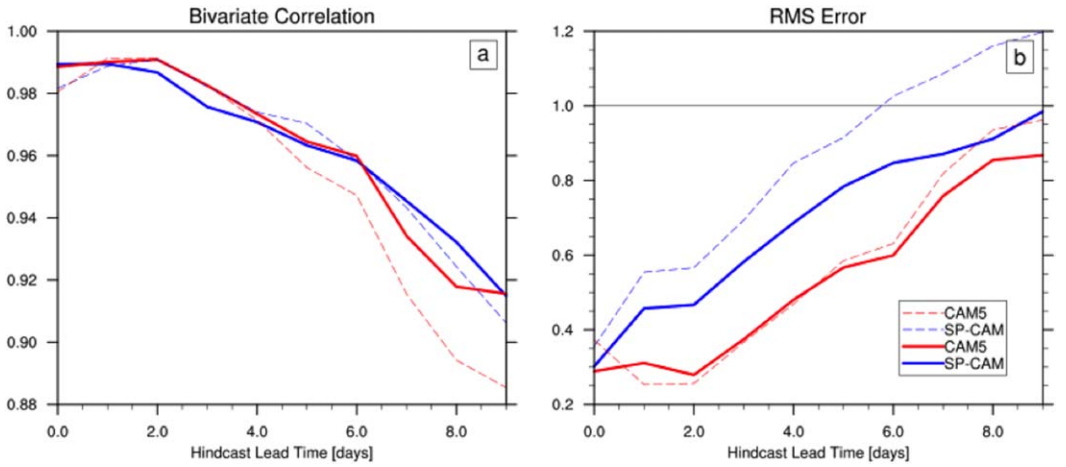

Figure 13. Similar to Figure 6, but with drift corrected (solid) and original (thin dashed) (left) COR and (right) RMSE RMM skill scores as a function of lead time in days for SP-CAM (blue) and CAM5 (red).

anything about what drives the MJO, and so our results regarding drift and the RMM do not directly give us any physical insight about this important question. Many studies have suggested that moisture is important to MJO dynamics, by modulating how convection is coupled with large-scale dynamics. To discuss the model drift in a more physically relevant context we will now consider how model drift can influence the column-integrated moisture budget of the DYNAMO hindcasts in SP-CAM and CAM5.

4.1. Analysis of Moisture Budget Drift

The longitudinal drift pattern of column-integrated water vapor (CWV) is shown in Figure 14. The patterns are qualitatively similar between the two models and indicate CWV changes of 2–3 mm over 10 days. The rate of column moistening leading up to the DYNAMO MJO events is roughly 1–2 mm d^{-1}, so the net drift tendencies are roughly 10% of the those associated with the MJO. However, as we will show, indivdual processes that make up this net tendency are naturally much larger, and so the drift of processes that control the column moisture budget are, arguably, not negligible to MJO moisture dynamics.

Figure 15 shows an alternate view of moisture drift by comparing the frequency distribution of CWV over the Indian and West Pacific Oceans (20°S–20°N; 40°E–180°E) in the first 2 days and last 2 days of the hindcasts. The CWV distribution in SP-CAM stays close to that in the ECMWF analysis throughout the 10 day hindcast, with a few slight exceptions. CAM5 hindcasts exhibit an interesting "contraction" of the moisture distrbution, in which there are fewer values at the extremes of the distribution by days 8–9 (Figure 15b). The wet and dry phases of the MJO are associated with changes in the shape of the CWV distribution (not shown), which are associated with the modulation of the large-scale convective activity. Given that the convective characteristics of the MJO appear to be fundamental to its dynamics, the change in the CAM5 CWV

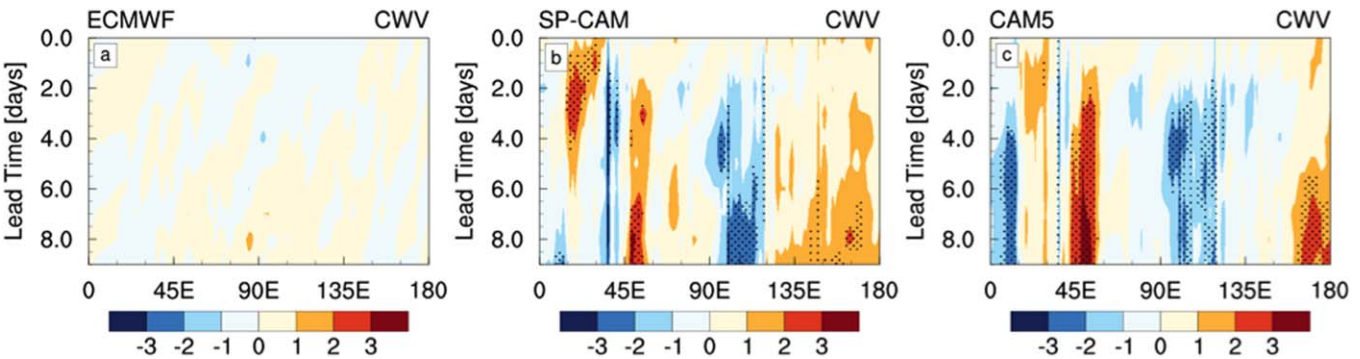

Figure 14. Hovmoller of column water vapor drift relative to ECMWF data. Data were averaged from 20°S to 20°N.

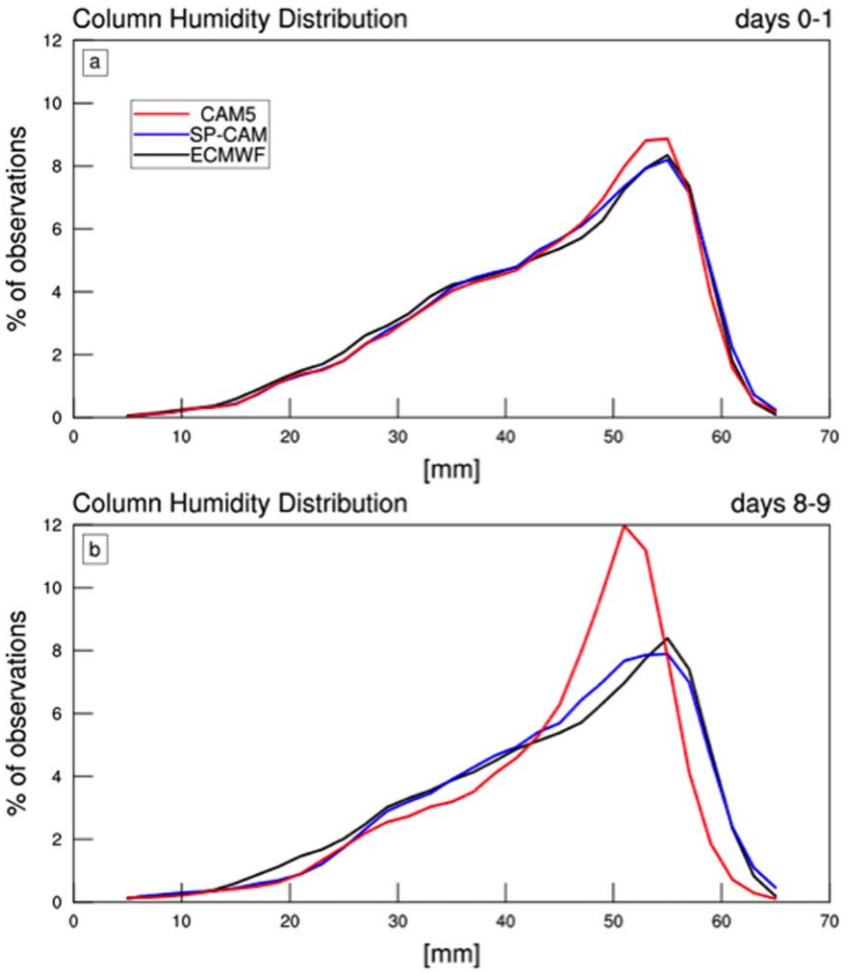

Figure 15. Frequency distribution of column water vapor for the (top) first and (bottom) last 2 days of the hindcast periods, for the Indian and West Pacific Ocean regions (20°S–20°N; 40°E–180°E). Data have been normalized by the total number of observations and multiplied by 100, so that the units can be shown as a percent.

distribution is arguably a more relevant discrepancy to the prediction of the MJO than the drift of large-scale wind patterns in SP-CAM that were shown to be so influential to the RMM skill scores.

The vertically integrated budget of water vapor can be approximated as,

$$\langle \partial_t q \rangle = -\langle \mathbf{v} \cdot \nabla q \rangle - \langle \omega \partial_p q \rangle + E - P, \tag{5}$$

where q is specific humidity, $\mathbf{v}$ is the horizontal wind, ω is vertical pressure velocity, E is surface evaporation, and P is precipitation. Angle brackets denote a mass weighted vertical integral throughout the troposphere. Following *Yanai et al*. [1973], we can also write the column moisture budget as

$$\langle \partial_t q \rangle = -\langle \mathbf{v} \cdot \nabla q \rangle - \langle \omega \partial_p q \rangle - \langle Q_2 \rangle, \tag{6}$$

where $\langle Q_2 \rangle$ is the column-integrated apparent moisture sink defined as the residual of the total derivative of q. Note that the units of our definition of Q_2 differ from that of *Yanai et al*. [1973], but this can be converted by dividing our Q_2 by the latent heat of vaporization. The ECMWF analysis used in this study provides data at 6 h intervals, except for forecasted variables, such as surface evaporation and precipitation, which are only available on 12 h intervals. Preliminary estimates of moisture budget terms revealed that the budget is better constrained with 4X daily data, compared to 2X or 1X daily data (not shown). For this reason we will only consider the budget as shown in (6) using 6 h data. It is also worth noting that the ECMWF data were interpolated to the model grid before calculating advective tendencies, as this ensures the resolved moisture gradients are of similar magnitude.

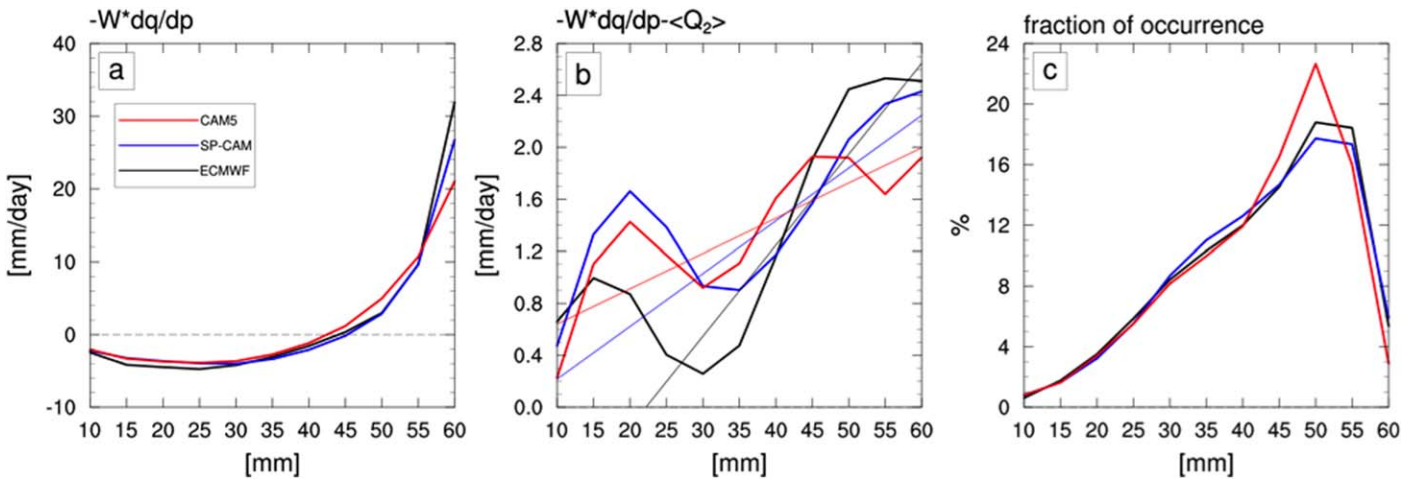

Figure 16. (a) Column-integrated vertical advection of water and (b) the sum of vertical advection and the apparent moisture sink binned by CWV anomaly using only data with 00–04 day lead times. Thin straight lines in Figure 16b show the result of linear regression analysis on the data (see text). The right figure shows the distribution of anomalous CWV. Data were restricted to the Indian and West Pacific Ocean regions (20°S–20°N; 40°E–180°E).

Figure 16a shows the tendency of CWV due to vertical advection binned by the CWV for 00–04 day lead times over the Tropical Indian Ocean and western Pacific Ocean (20°S–20°N; 40°E–180°E). Vertical advection acts to dry out the column in dry conditions due to subsidence, and moisten the column in moist conditions due to large-scale upward motion. This is consistent with the relationship of precipitation and column water in previous studies [*Bretherton et al*., 2004; *Neelin et al*., 2009; *Sahany et al*., 2012]. The CWV tendency due to vertical advection is large compared to horizontal advection in the Tropics, but is largely cancelled by diabatic processes represented by $\langle Q_2 \rangle$, such as moist convection [*Chikira*, 2014]. The residual of vertical advection and $\langle Q_2 \rangle$ is much smaller than vertical advection alone (Figure 16b), and generally balances the total horizontal advection (Figure 17a). Comparing this quantity between hindcasts and observations, the models exhibit a stronger moistening tendency in dry environments (Figure 16b). For wetter environments, CAM5 has much weaker moistening compared to ECMWF, which would restrict the models' ability to maintain high CWV values. SP-CAM more closely matches the ECMWF analysis at the high CWV values.

We can get a sense of the overall strength of moisture-convection feedbacks from linear regression of CWV and the sum of vertical advection and $\langle Q_2 \rangle$ (thin straight lines in Figure 16b). The regression slope is positive in all casese, implying that the net effects of convection and divergent circulations provide stronger moistening as CWV increases. Both models have a less positive regression slope than ECMWF, but SP-CAM is more positive than CAM5. Thus, we can conlcude that CAM5 has weaker moisture-convection feedbacks

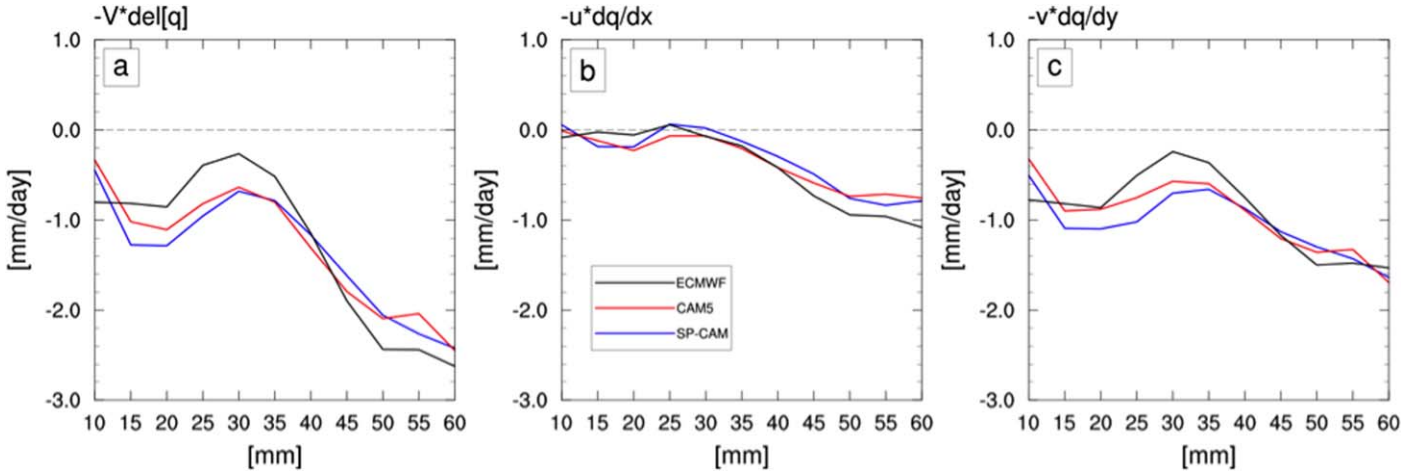

Figure 17. Terms of the CWV budget binned by CWV anomaly, similar to Figure 16, except for (a) total advection, (b) zonal advection, and (c) meridional advection.

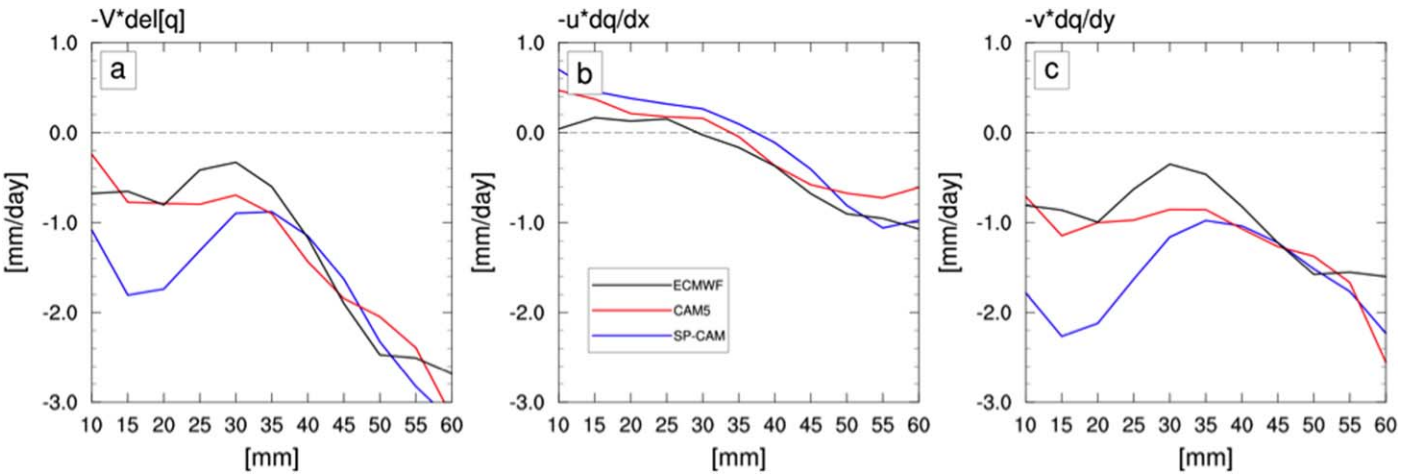

Figure 18. Similar to Figure 17, except for 05–09 day lead times.

compared to SP-CAM. This may help explain the contraction of the moisture distribution in CAM5, because it is less able to develop and maintain large moisture anomalies (Figure 15). Similar conclusions can be drawn from similar analysis of 05–09 day lead times (not shown).

Figure 17 shows a breakdown of the horizontal advective tendency of CWV, binned by CWV for 00–04 day lead times. Horizontal advection generally contributes a drying tendency, which is strongest for the wettest columns (Figure 17a). In moist environments above 45 mm, both models show less drying, which comes from differences in the zonal component (Figure 17b). In dry environments between 20 and 45 mm, both models show stronger drying by advection that can be attributed to the meridional component (Figure 17c). Interestingly, the bias in meridional advection becomes larger in SP-CAM at later lead times (Figure 18c).

In order to put the above results in context of the MJO we can examine the spatial pattern of the drift of CWV budget terms. Figures 19 and 20 show hovmoller plots of these drift patterns calculated with ECMWF as a reference similar to Figure 9. Note that Figures 19a and 20a are included to show that there is no coherent drift in ECWMF data. In both models, the drift of vertical advection has a coherent pattern that would tend to moisten over the Western Indian and West Pacific oceans, and dry over the Eastern Indian Ocean (Figures 19b and 19c). The drift of the net tendency by vertical advection and diabatic sources shows a moistening pattern similar to vertical advection, but it is smaller in magnitude, and contributes a positive tendency in most regions. This moistening rate reaches 2 mm d^{-1} in the Western Indian Ocean in SP-CAM, and is somewhat smaller in CAM5. Given that the convective signal of the MJO initiates in Western Indian Ocean, this drift of the moisture tendencies could have a significant impact on the ability of the model to correctly reproduce the timing of MJO initiation.

Figure 20 shows the drift pattern of zonal (Figures 20a–20c) and merdional (Figures 20d–20f) horizontal advective tendencies. The drift of zonal advection in SP-CAM contributes larger tendencies than CAM5. The pattern of zonal advection does not have a coherent large-scale structure, which is surprising given the coherent wind drift patterns discussed in section 3 (Figure 9). On the other hand, meridional wind shows a coherent large-scale drift pattern in SP-CAM hindcasts (Figure 20e), with drying that steadily increases in the vicinity of the Maritime continent and the Western Indian Ocean, consistent with Figure 18. This drying in the Western Indian Ocean is compensated by an increase in the sum of vertical advection and $\langle Q_2 \rangle$ (Figure 19e). However, the increased meridional advective drying between 90° and 120° does not have a corresponding compensation.

4.2. Drift of Synoptic Eddy Activity

The meridonal moisture advection drift pattern in SP-CAM (Figure 20e) appears to be unique and is continually amplifying with lead time, so it is worth further investigation. The drift patterns of other budget terms do not have coherent evolving structures, and therefore are not straighforward to explain. However, a possible explanation for the meridional advection drift comes from *Maloney* [2009], who showed that advection

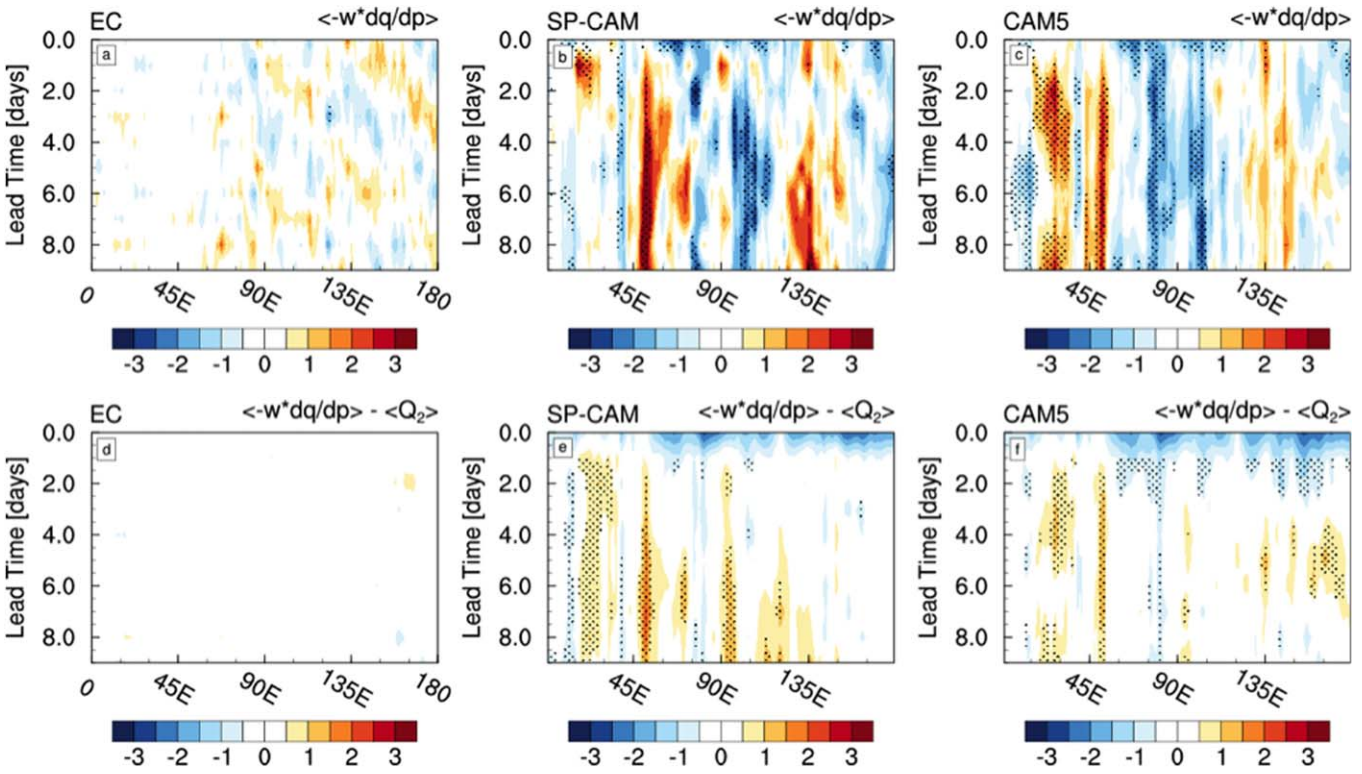

Figure 19. (a–c) Hovmoller drift of the vertical advective tendency and (d–f) the sum of vertical advection and the CWV budget residual relative to ECMWF data. Data were averaged from 20°S to 20°N. Stippling indicates where the drift signal is significantly different than zero at the 95% cofidence level. Note that positive values indicate moistening.

by synoptic eddies explained a large part of the meridional moist static energy advection of the MJO in a global model [*Pritchard and Bretherton*, 2014; *Landu and Maloney*, 2011; *Andersen and Kuang*, 2012]. Thus, an enhancement of off-equatorial eddy activity that amplifies with lead time would also affect the meridonal moisture advection (Figure 20e).

To address the hypothesis that meridonal advection is influenced by an enhancement of eddy activity with lead time, it would be convienient to use a measure of eddy kinetic energy (EKE) such as,

$$EKE = \frac{\overline{u'^2 + v'^2}}{2}, \tag{7}$$

where the bar and primes denote a temporal window mean and deviations from that mean, respectively. This would identify eddies and also allows us to explain their generation by various source terms in the eddy kinetic energy budget [*Lau and Lau*, 1992; *Alaka and Maloney*, 2014]. However, this is problematic in a 10 day hindcasts, because we do not have enough data to filter properly. If we use a 5 day running mean we lose 4 days out of each hindcast, and a shorter running mean would not effectively isolate the eddy circulations from the mean. Therefore, we are forced to use indirect methods of testing our hypothesis.

Instead of EKE, we will use a basic kinetic energy (KE), defined as,

$$KE = \frac{u^2 + v^2}{2}. \tag{8}$$

Figure 21 shows a map of 700 hPa KE drift relative to ECMWF data averaged over the last 2 days of each hindcast (i.e., days 8 and 9), with contours of CWV overlayed. Much of the KE drift signal appears to be organized on synoptic scales in both models. SP-CAM shows much larger and widespread KE anomalies compared to CAM5. SP-CAM also shows a strong KE enhancement on the meridional moisture gradient north of the equator in the Indian Ocean (Figure 21), which is consistent with the drying by meridional advection (Figure 20e).

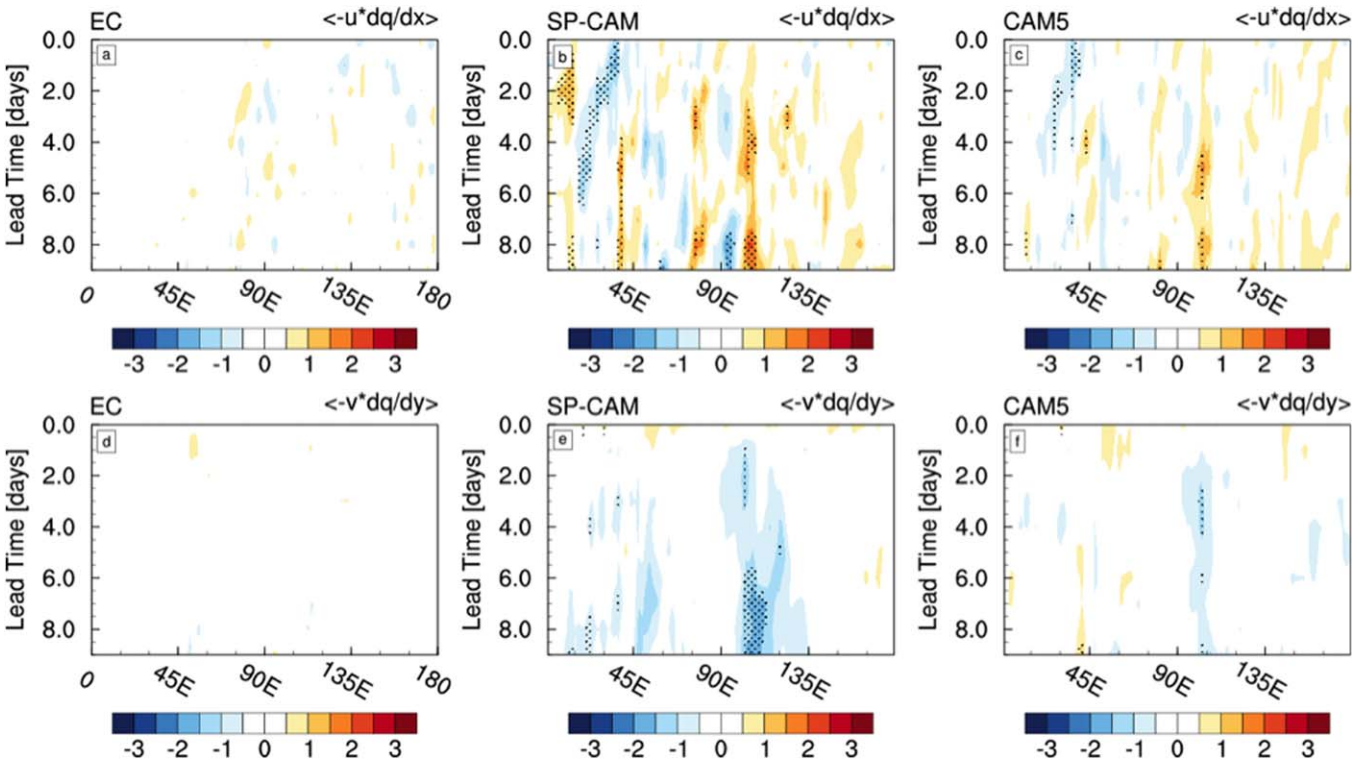

Figure 20. Similar to Figure 19, except for (a–c) zonal and (d–f) meridional advective tendencies of CWV relative to ECMWF data.

In order to quantify the scale selection of the KE drift pattern, we can calculate a spatial fourier transform that yields the zonal wavenumber power spectrum of KE, and then calculate the drift of this spectrum relative to ECMWF. To do this, KE spectra are calculated separately for each day and latitude band, and then averaged to yield the KE drift as a function of lead time and zonal wavenumber. We restrict the data to 10°N–20°N to capture the eddies that mix across the mean moisture gradient north of the equator, and are presumably responsible for the drift of merdional moisture advection. Note that this analysis requires a periodic domain, so it cannot be restricted to a region such as the Indian Ocean.

Figure 22 shows drift of the KE wavenumber power spectrum as a function of lead time calculated relative to the time average spectral power of ECMWF data in each band. This analysis shows that the KE drift in SP-CAM hindcasts preferentially occurs on synoptic scales (10^3-10^4 km), whereas CAM5 hindcasts do not show any notable drift. To test whether this result is statistically significant, we can use the *F* test for the null hypothesis that two populations have equal variance. The test statistic is defined as the ratio of two variances, s_1^2 and s_2^2, from normally distributed populations as,

$$F = \frac{s_1^2}{s_2^2}. \tag{9}$$

In our case we need only calculate the ratio of two spectral estimates in each wavenumber band. Since we are expecting a drift signal in synoptic bands of the spectrum a priori [see *Madden and Julian*, 1971], we can simply use a critical *F* value from a lookup table. Using a very conservative estimate of 30 degrees of reedom, the appropriate critical *F* value is 1.84. The stipling in Figure 22 designates where the *F*-statistic exceeds the critical value, indicating that the synoptic wave activity in SP-CAM is systematically enhanced and becomes statistically distinct starting around days 3–5 of the hindcasts.

Even though we cannot analyze the EKE budget to understand the drift pattern of moisture advection, we can find qualitative evidence of the mechanism at play. Figure 23 shows the zonal wind drift pattern averaged zonally over 60°E–150°E (shading), along with the time mean zonal wind (contours). There are many interesting upper level features, such as the tendency for SP-CAM to shift the southern subtropical jet poleward. At low levels, where the change in moisture advection is most dramatic (not shown), the drift pattern

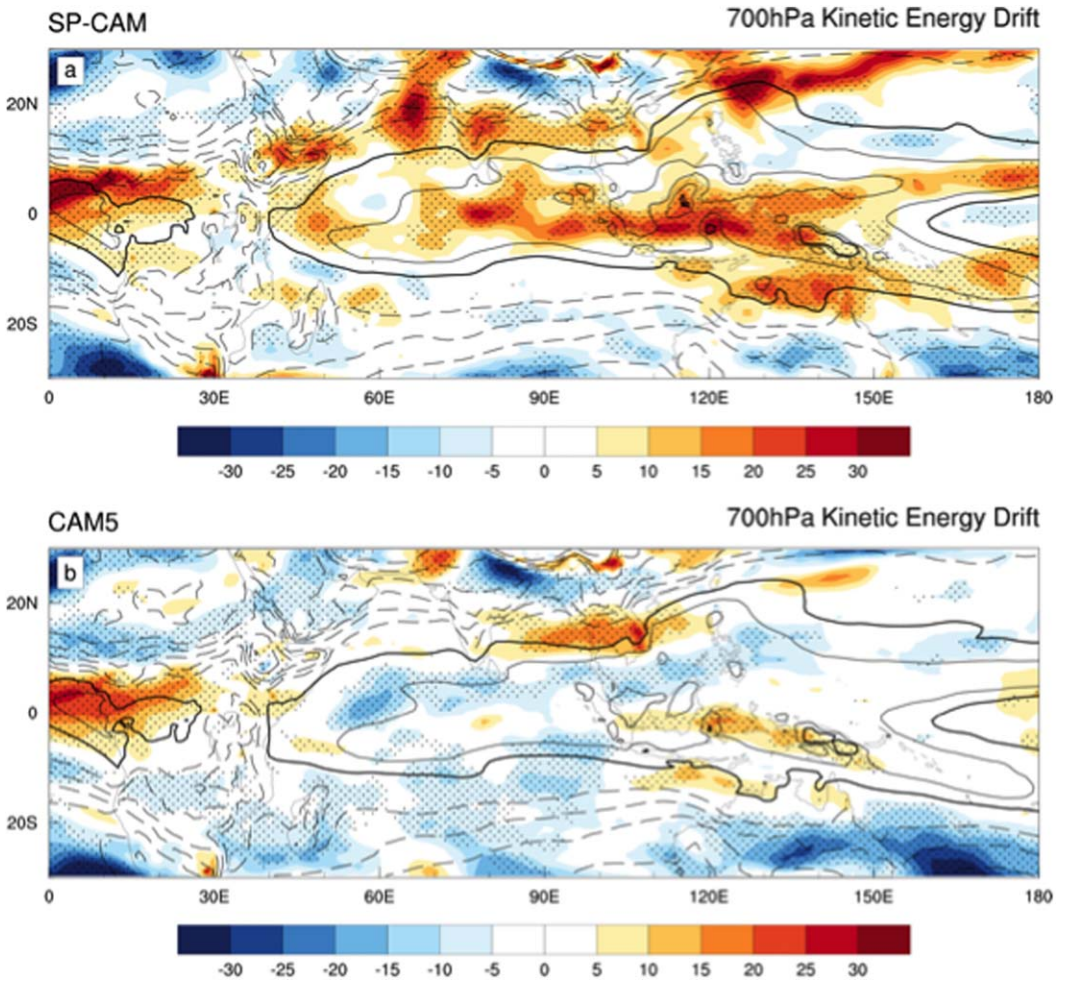

Figure 21. Spatial drift pattern of 700 hPa kinetic energy averaged over the last 2 days of the hindcasts. Kinetic energy is shown in units of $m^2\ s^{-2}$. Contours show the mean CWV at intervals of 5 mm, with contours less than 45 mm dashed.

of zonal wind acts to amplify the westerlies on the equator, as well as the easterlies to the north of the equator. This enhances the shear zone around 0°N–15°N, which roughly coincides with the location of the enhanced synoptic-scale KE (Figure 20). The drift patterns in CAM5 are qualitatively similar, but not as dramatic, consistent with the lack of systematic synoptic KE enhancement.

5. Conclusions and Discussion

5.1. Summary

Hindcast simulations of the first two MJO events during the DYNAMO field campaign are performed with SP-CAM and CAM5, and evaluated against analysis and satellite data. SP-CAM produces a better mean precipitation pattern (Figure 1), and a somewhat more robust MJO convective signal than CAM5 (Figures 2 and 3). Despite these qualitative results, RMM skill scores suggest that SP-CAM has less skill reproducing the observed RMM amplitude than CAM5 (Figure 6). Closer inspection shows that systematic drift in SP-CAM fields projects positively onto RMM1 and negatively onto RMM2, which heavily influences RMM skill scores (Figure 11). The RMM bias in SP-CAM is mostly caused by the drift of 850 hPa zonal wind, but the drift of 200 hPa zonal wind and outgoing longwave radiation (OLR) also have a noticeable impact on RMM skill scores. A naïve attempt to remove the systematic drift in the hindcasts alters the RMM skill scores, but SP-CAM still has an amplitude bias relative to CAM5, which is likely related to the overestimation of wind anomalies in SP-CAM. These results shed light on how a model with a good MJO can have poor MJO forecasts [*Klingaman et al*., 2015].

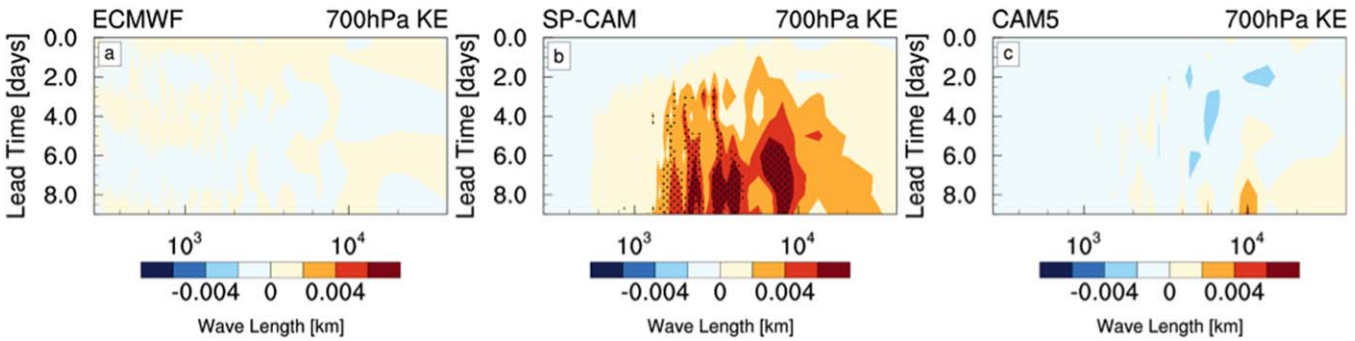

Figure 22. Drift of kinetic energy wavenumber power spectrum as a function of lead time. Data for this analysis were restricted to 10°N–20°N and necessarily includes all longitudes. Fourier analysis was performed separately on each longitude band before averaging the power spectra together. Stippling indicates statistical significance of the spectral difference at the 95% cofidence level based on an *F* test (see text).

Both models exhibit a coherent drift pattern of the equatorial Indian Ocean column water vapor (CWV; Figures 14 and 15). Analysis of the CWV budget for small lead times shows that the combined effects of vertical advection and diabatic processes moisten too much in dry regimes and too little in the wettest regimes in both models (Figure 16). This issue is particularly prevalent in CAM5, and linear regression analysis further suggests that CAM5 has weaker overall moisture-convection feedbacks than SP-CAM. Horizontal advection also has an interesting bias, in which meridional advection dries too much in dry regimes and zonal advection dries too little in the wettest regimes (Figure 17).

Drift of CWV budget terms reveals some interesting systematic patterns. The drift of tendencies by vertical advection and diabatic processes shows systematic moistening in the western Indian Ocean and West Pacific, which could affect the prediction skill of dry phase conditions (Figure 19). A systematic increase in drying by meridional advection in SP-CAM (Figure 20) seems to be associated with an increase in off-equatorial synoptic eddy activity that occurs in the vicinity of strong meridional moisture gradients (Figures 21 and 22). The data do not permit a thorough analysis of the eddy kinetic energy budget, but the drift of zonal wind suggests that barotropic energy conversion from an enhanced off-equatorial shear zone may be able to explain the increase in synoptic eddy activity (Figure 23).

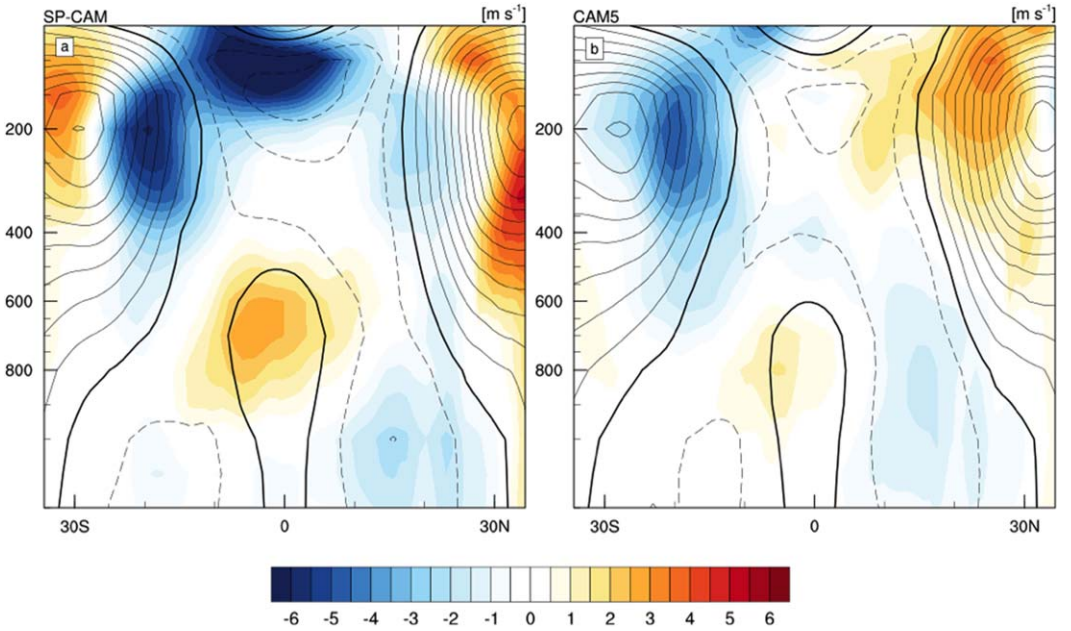

Figure 23. Zonally averaged zonal wind (contours) and zonal wind drift (shaded). Data were averaged over 60°E–150°E.

The drift of these moisture tendencies are not negligible to MJO moisture dynamics. Previous studies that analyzed the column moist static energy and moisture budgets found anomalous column moist static energy tendencies on the order of 20 W m^{-2}, which corresponds to less than 1 mm d^{-1} CWV tendency [*Maloney*, 2009; *Landu and Maloney*, 2011; B. O. Wolding and E. D. Maloney, Objective diagnostics and the Madden-Julian oscillation. Part II: Application to moist static energy and moisture budgets, submitted to *Journal of Climate*, 2015]. The magnitude of CWV tendency drift in SP-CAM from advection and diabatic processes discussed here are similar to these previous studies, and therefore have serious implications for MJO prediction skill.

5.2. Discussion

The findings here are useful for understanding model shortcomings and can be abridged into two main conclusions. The first being that systematic drift of MJO hindcast experiments can distort RMM skill scores. This highlights one of several weaknesses of the RMM index that have been discussed by recent studies [*Straub*, 2013; *Kiladis et al*., 2014]. The second conclusion is that a superparameterized model can do a comparable or better job reproducing the convective signal of the MJO than a conventional model, while still having similar moisture budget biases (Figures 16 and 17), as well as drift of the moisture budget terms (Figures 19 and 20).

A noteworthy caveat of our conclusions about the moisture budget is that we are comparing a model to an analysis product, which is largely influenced by parameterized model physics in data-sparse regions, like the Indian Ocean. *Mapes and Bacmeister* [2012] provided a detailed description of the analysis tendencies of the model used for the Modern Era Reanalysis (MERRA) product, as this indicates when and where assimilation corrections are needed to compensate for model errors. Analysis tendencies of MERRA MJO events showed a moistening correction during the moistening period that precedes the convectively active phase, indicating that the model was far too dry. If the analysis used here has similar issues, then our conclusions regarding Figures 16–20 require a caveat. There is evidence that this is the case, as *Landu and Maloney* [2011] found a budget residual during the MJO moistening period in ECMWF interim reanalysis similar to what *Mapes and Bacmeister* [2012] found for MERRA. Nonetheless, ECMWF analysis is currently one of the best resources for investigating the dynamics of the MJO at the larger scales during DYNAMO.

There are many possible methods of addressing the issue of model drift [*Judd et al*., 2008], but this can be a complicated task that will be out of scope for most model based studies of the MJO. Perhaps this means that hindcast experiments should be limited to models that have a trusted data assimilation structure in place [*Raeder et al*., 2012]. Either way, we have shown that SP-CAM can produce a robust hindcasts of observed MJO events, so the issues surrounding model drift and the corresponding effects on MJO dynamics may, ultimately, not be of first-order importance at this time. On the other hand, the impacts of drift on the RMM are very large and should not be ignored. Better metrics that are not prone to the projection issues outlined here would benefit both operational and scientific interests.

So if the RMM has flaws in assessing MJO forecast skill, what is the alternative? This is a somewhat indirect way of asking, "What is the MJO?" If we possessed a deep understanding of the fundamental dynamics of the MJO, then we should be able to tell how well a model can reproduce it based on "process-oriented" diagnostics. The RMM index is not process-oriented, because it empirically identifies relevant wind and OLR patterns which fluctuate on the appropriate time scale, rather than building on an understanding of what makes the MJO tick.

The theory of "moisture modes" offers a promising explanation of some observed characteristics of the MJO [*Sobel et al*., 2001; *Raymond and Fuchs*, 2009] that could be used to create a process-oriented MJO index. An index designed to identify moisture modes would obviously involve the spatial distribution of moisture, but might also include details of how various processes are changing column moisture. For example, if the location of evaporation anomalies relative to the area of enhanced moisture are crucial for the maintenance of the MJO, an index that includes this could help identify the potential for long-lived events. Details about the presence of cloud populations that amplify or damp column moisture could also be included to better predict MJO initiation. Ideally, this approach would consider consequences of weak-temperature gradient balance, such as how radiative heating can influence moisture [*Chikira*, 2014]. The drift of the column

moisture distribution in CAM5 (Figure 15) suggests that such a process-oriented approach to MJO forecast skill would implicate SP-CAM as the superior model to CAM5. Current work is under way to develop a set of metrics to this end.

Acknowledgments

The authors would like to thank Jerry Olson and Richard Neale at NCAR and Gabe Kooperman at UC Irvine for help with setting up the CESM hindcasts. This work was supported by the Climate and Large-Scale Dynamics Program of NSF under grants AGS-1062161, AGS-1025584, and AGS-1441916 and the Science and Technology Center for Multi-Scale Modeling of Atmospheric Processes, managed by Colorado State University under cooperative agreement ATM-0425247. This work has also been funded by award NA13OAR4310163 from NOAA, U.S. Department of Commerce and by the Department of Energy under award DE-SC0012152. All data from this study are available upon request to the primary author by e-mailing walter@hannahlab.org. The statements, findings, conclusions, and recommendations do not necessarily reflect the views of NSF, NOAA, or the Department of Commerce.

References

Alaka, G. J., and E. D. Maloney (2012), The influence of the MJO on upstream precursors to African easterly waves, *J. Clim.*, *25*, 3219–3236.

Alaka, G. J., and E. D. Maloney (2014), The intraseasonal variability of African easterly wave energetics, *J. Clim.*, *27*, 6559–6580.

Andersen, J. J. A. J., and Z. Kuang (2012), Moist static energy budget of MJO-like disturbances in the atmosphere of a zonally symmetric aquaplanet, *J. Clim.*, *25*, 2782–2804.

Bechtold, P., M. Köhler, T. Jung, F. Boblas-Reyes, M. Leutbecher, M. J. Rodwell, F. Vitart, and G. Balsamo (2008), Advances in simulating atmospheric variability with the ECMWF model: From synoptic to decadal time-scales, *Q. J. R. Meteorol. Soc.*, *1351*, 1337–1351.

Benedict, J. J., and D. Randall (2009), Structure of the Madden-Julian oscillation in the superparameterized CAM, *J. Atmos. Sci.*, *66*, 3277–3296.

Benedict, J. J., and D. A. Randall (2011), Impacts of idealized air–sea coupling on Madden–Julian oscillation structure in the superparameterized CAM, *J. Atmos. Sci.*, *68*, 1990–2008.

Benedict, J. J., E. D. Maloney, A. H. Sobel, and D. M. W. Frierson (2014), Gross moist stability and MJO simulation skill in three full-physics GCMs, *J. Atmos. Sci.*, *71*, 3327–3349.

Bretherton, C., and S. Park (2009), A new moist turbulence parameterization in the Community Atmosphere Model, *J. Clim.*, *22*, 3422–3448.

Bretherton, C., M. Peters, and L. Back (2004), Relationships between water vapor path and precipitation over the tropical oceans, *J. Clim.*, *17*, 1517–1528.

Cassou, C. (2008), Intraseasonal interaction between the Madden-Julian oscillation and the North Atlantic oscillation, *Nature*, *455*, 523–527.

Chikira, M. (2014), Eastward-propagating intraseasonal oscillation represented by Chikira–Sugiyama cumulus parameterization. Part II: Understanding moisture variation under weak temperature gradient balance, *J. Atmos. Sci.*, *71*, 615–639.

DeMott, C. A., C. Stan, D. A. Randall, and M. D. Branson (2014), Intraseasonal variability in coupled GCMs: The roles of ocean feedbacks and model physics, *J. Clim.*, *27*, 4970–4995.

Ding, R., J. Li, and K.-H. Seo (2010), Predictability of the Madden–Julian oscillation estimated using observational data, *Mon. Weather Rev.*, *138*, 1004–1013.

Feddersen, H., A. Navarra, and M. N. Ward (1999), Reduction of model systematic error by statistical correction for dynamical seasonal predictions, *J. Clim.*, *12*, 1974–1989.

Gottschalck, J., et al. (2010), A framework for assessing operational Madden–Julian oscillation forecasts: A CLIVAR MJO working group project, *Bull. Am. Meteorol. Soc.*, *91*, 1247–1258.

Grabowski, W. W., and M. W. Moncrieff (2004), Moisture–convection feedback in the tropics, *Q. J. R. Meteorol. Soc.*, *130*, 3081–3104.

Hannah, W. M., and E. D. Maloney (2011), The role of moisture-convection feedbacks in simulating the Madden-Julian oscillation, *J. Clim.*, *24*, 2754–2770.

Hannah, W. M., and E. D. Maloney (2014), The moist static energy budget in NCAR CAM5 hindcasts during DYNAMO, *J. Adv. Model. Earth Syst.*, *6*, 420–440, doi:10.1002/2013MS000272.

Hendon, H., and B. Liebmann (1990), The intraseasonal (30–50 day) oscillation of the Australian summer monsoon, *J. Atmos. Sci.*, *47*, 2909–2923.

Huang, B., Z.-Z. Hu, and B. Jha (2007), Evolution of model systematic errors in the tropical Atlantic basin from coupled climate hindcasts, *Clim. Dyn.*, *28*, 661–682.

Johnson, R. H., and P. E. Ciesielski (2013), Structure and properties of Madden–Julian oscillations deduced from DYNAMO sounding arrays, *J. Atmos. Sci.*, *70*, 3157–3179.

Joseph, S., A. K. Sahai, and B. N. Goswami (2008), Eastward propagating MJO during boreal summer and Indian monsoon droughts, *Clim. Dyn.*, *32*, 1139–1153.

Judd, K., C. A. Reynolds, T. E. Rosmond, and L. A. Smith (2008), The geometry of model error, *J. Atmos. Sci.*, *65*, 1749–1772.

Jung, J., and A. Arakawa (2005), Preliminary tests of multiscale modeling with a two-dimensional framework: Sensitivity to coupling methods, *Mon. Weather Rev.*, *133*, 649–662.

Jung, T. (2005), Systematic errors of the atmospheric circulation in the ECMWF forecasting system, *Q. J. R. Meteorol. Soc.*, *131*, 1045–1073.

Kanamitsu, M., W. Ebisuzaki, J. Woollen, S.-K. Yang, J. J. Hnilo, M. Fiorino, and G. L. Potter (2002), NCEP–DOE AMIP-II Reanalysis (R-2), *Bull. Am. Meteorol. Soc.*, *83*, 1631–1643.

Kang, I.-S., J.-Y. Lee, and C.-K. Park (2004), Potential predictability of summer mean precipitation in a dynamical seasonal prediction system with systematic error correction, *J. Clim.*, *17*, 834–845.

Khairoutdinov, M., and D. Randall (2001), A cloud resolving model as a cloud parameterization in the NCAR community climate system model: Preliminary results, *Geophys. Res. Lett.*, *28*, 3617–3620.

Khairoutdinov, M., and D. Randall (2003), Cloud resolving modeling of the ARM summer 1997 IOP: Model formulation, results, uncertainties, and sensitivities, *J. Atmos. Sci.*, *60*, 607–625.

Khairoutdinov, M. F., D. A. Randall, and C. A. DeMott (2005), Simulations of the atmospheric general circulation using a cloud-resolving model as a superparameterization of physical processes, *J. Atmos. Sci.*, *62*, 2136–2154.

Kiladis, G. N., J. Dias, K. H. Straub, M. C. Wheeler, S. N. Tulich, K. Kikuchi, K. M. Weickmann, and M. J. Ventrice (2014), A comparison of OLR and circulation based indices for tracking the MJO, *Mon. Weather Rev.*, *142*, 1697–1715.

Kim, D., et al. (2009), Application of MJO simulation diagnostics to climate models, *J. Clim.*, *22*, 6413–6436.

Kim, D., et al. (2014), Process-oriented MJO simulation diagnostic: Moisture sensitivity of simulated convection, *J. Clim.*, *27*, 5379–5395.

Kim, H.-M., P. J. Webster, V. E. Toma, and D. Kim (2014), Predictability and prediction skill of the MJO in two operational forecasting systems, *J. Clim.*, *27*, 5364–5378.

Klingaman, N. P., and S. J. Woolnough (2014), Using a case-study approach to improve the Madden-Julian oscillation in the Hadley centre model, *Q. J. R. Meteorol. Soc.*, *140*, 2491–2505.

Klingaman, N. P., et al. (2015), Vertical structure and diabatic processes of the Madden–Julian oscillation: Linking hindcast fidelity to simulated diabatic heating and moistening, *J. Geophys. Res. Atmos.*, *120*, 1–28, doi:10.1002/2014JD022374.

Landu, K., and E. D. Maloney (2011), Intraseasonal moist static energy budget in reanalysis data, *J. Geophys. Res.*, *116*, D21117, doi:10.1029/2011JD016031.

Lau, K., and N. Lau (1992), The energetics and propagation dynamics of tropical summertime synoptic-scale disturbances, *Mon. Weather Rev.*, *120*, 2523–2539.
Liebmann, B., and C. A. Smith (1996), Description of a complete (interpolated) outgoing longwave radiation datasets, *Bull. Am. Meteorol. Soc.*, *77*, 1275–1277.
Lin, H., G. Brunet, and J. Derome (2008a), Forecast skill of the Madden–Julian oscillation in two Canadian atmospheric models, *Mon. Weather Rev.*, *136*, 4130–4149.
Lin, J., et al. (2006), Tropical intraseasonal variability in 14 IPCC AR4 climate models. Part I: Convective signals, *J. Clim.*, *19*, 2665–2690.
Lin, J.-L., M.-I. Lee, D. Kim, I.-S. Kang, and D. M. W. Frierson (2008b), The impacts of convective parameterization and moisture triggering on AGCM-simulated convectively coupled equatorial waves, *J. Clim.*, *21*, 883–909.
Ling, J., P. Bauer, P. Bechtold, A. Beljaars, R. Forbes, F. Vitart, M. Ulate, and C. Zhang (2014), Global versus local MJO forecast skill of the ECMWF model during DYNAMO, *Mon. Weather Rev.*, *142*, 2228–2247.
Lorenz, E. N. (1968), The predictability of a flow which possesses many scales of motion, *Tellus*, *21*, 289–307.
Luo, Z., and G. L. Stephens (2006), An enhanced convection-wind-evaporation feedback in a superparameterization GCM (SP-GCM) depiction of the Asian summer monsoon, *Geophys. Res. Lett.*, *33*, L06707, doi:10.1029/2005GL025060.
Ma, H.-Y., S. Xie, J. S. Boyle, S. A. Klein, and Y. Zhang (2013), Metrics and diagnostics for precipitation-related processes in climate model short-range hindcasts, *J. Clim.*, *26*, 1516–1534.
Madden, R., and P. Julian (1971), Detection of a 40–50 day oscillation in the zonal wind in the tropical pacific, *J. Atmos. Sci.*, *28*, 702–708.
Madden, R. A., and P. R. Julian (1972), Description of global-scale circulation cells in the tropics with a 40–50 day period, *J. Atmos. Sci.*, *29*, 1109–1123.
Maloney, E. D. (2009), The moist static energy budget of a composite tropical intraseasonal oscillation in a climate model, *J. Clim.*, *22*, 711–729.
Maloney, E. D., and D. Hartmann (2001), The sensitivity of intraseasonal variability in the NCAR CCM3 to changes in convective parameterization, *J. Clim.*, *14*, 2015–2034.
Mapes, B. E., and J. T. Bacmeister (2012), Diagnosis of tropical biases and the MJO from patterns in the MERRA analysis tendency fields, *J. Clim.*, *25*, 6202–6214.
Mapes, B. E., S. Tulich, T. Nasuno, and M. Satoh (2008), Predictability aspects of global aqua-planet simulations with explicit convection, *J. Meteorol. Soc. Jpn.*, *86A*, 175–185.
Marshall, A. G., D. Hudson, M. C. Wheeler, H. H. Hendon, and O. Alves (2010), Assessing the simulation and prediction of rainfall associated with the MJO in the POAMA seasonal forecast system, *Clim. Dyn.*, *37*, 2129–2141.
Matthews, A. (2004), Intraseasonal variability over tropical Africa during northern summer, *J. Clim.*, *17*, 2427–2440.
Morrison, H., and A. Gettelman (2008), A new two-moment bulk stratiform cloud microphysics scheme in the community atmosphere model, version 3 (CAM3). Part I: Description and numerical tests, *J. Clim.*, *21*, 3642–3659.
Neale, R. B., et al. (2010), Description of the NCAR community atmosphere model (CAM 5.0), *NCAR Tech. Note NCAR/TN-486+STR*, Natl. Cent. for Atmos. Res., Boulder, Colo.
Neelin, J. D., O. Peters, and K. Hales (2009), The transition to strong convection, *J. Atmos. Sci.*, *66*, 2367–2384.
Neena, J. M., J. Y. Lee, D. Waliser, B. Wang, and X. Jiang (2014), Predictability of the Madden–Julian oscillation in the intraseasonal variability hindcast experiment (ISVHE), *J. Clim.*, *27*, 4531–4543.
Park, S., and C. S. Bretherton (2009), The University of Washington shallow convection and moist turbulence schemes and their impact on climate simulations with the community atmosphere model, *J. Clim.*, *22*, 3449–3469.
Pavan, V., and F. J. Doblas-Reyes (2000), Multi-model seasonal hindcasts over the Euro-Atlantic: Skill scores and dynamic features, *Clim. Dyn.*, *16*, 611–625.
Phillips, T. J., G. L. Potter, D. L. Williamson, R. T. Cederwall, J. S. Boyle, M. Fiorino, J. J. Hnilo, J. G. Olson, S. Xie, and J. J. Yio (2004), Evaluating parameterizations in general circulation models: Climate simulation meets weather prediction, *Bull. Am. Meteorol. Soc.*, *85*, 1903–1915.
Pritchard, M. S., and C. S. Bretherton (2014), Causal evidence that rotational moisture advection is critical to the superparameterized Madden-Julian oscillation, *J. Atmos. Sci.*, *71*, 800–815.
Pritchard, M. S., C. S. Bretherton, and C. A. DeMott (2014), Restricting 32–128 km horizontal scales hardly affects the MJO in the superparameterized community atmosphere model v.3.0 but the number of cloud-resolving grid columns constrains vertical mixing, *J. Adv. Model. Earth Syst.*, *6*, 723–739, doi:10.1002/2014MS000340.
Raeder, K., J. L. Anderson, N. Collins, T. J. Hoar, J. E. Kay, P. H. Lauritzen, and R. Pincus (2012), DART/CAM: An ensemble data assimilation system for CESM atmospheric models, *J. Clim.*, *25*, 6304–6317.
Randall, D. A., M. Khairoutdinov, A. Arakawa, and W. Grabowski (2003), Breaking the cloud parameterization deadlock, *Bull. Am. Meteorol. Soc.*, *84*, 1547–1564.
Rashid, H. A., H. H. Hendon, M. C. Wheeler, and O. Alves (2010), Prediction of the Madden–Julian oscillation with the POAMA dynamical prediction system, *Clim. Dyn.*, *36*, 649–661.
Raymond, D. J., and Ž. Fuchs (2009), Moisture modes and the Madden–Julian oscillation, *J. Clim.*, *22*, 3031–3046.
Sahany, S., J. D. Neelin, K. Hales, and R. B. Neale (2012), Temperature–moisture dependence of the deep convective transition as a constraint on entrainment in climate models, *J. Atmos. Sci.*, *69*, 1340–1358.
Seo, K.-H., W. Wang, J. Gottschalck, Q. Zhang, J.-K. E. Schemm, W. R. Higgins, and A. Kumar (2009), Evaluation of MJO forecast skill from several statistical and dynamical forecast models, *J. Clim.*, *22*, 2372–2388.
Shi, L., H. H. Hendon, O. Alves, M. C. Wheeler, D. Anderson, and G. Wang (2010), On the importance of initializing the stochastic part of the atmosphere for forecasting the 1997/1998 El Niño, *Clim. Dyn.*, *37*, 313–324.
Slingo, J. M., et al. (1996), Intraseasonal oscillations in 15 atmospheric general circulation models: Results from an AMIP diagnostic subproject, *Clim. Dyn.*, *12*, 325–357.
Sobel, A. H., J. Nilsson, and L. M. Polvani (2001), The weak temperature gradient approximation and balanced tropical moisture waves, *J. Atmos. Sci.*, *58*, 3650–3665.
Stan, C., M. Khairoutdinov, C. A. DeMott, V. Krishnamurthy, D. M. Straus, D. A. Randall, J. L. Kinter, and J. Shukla (2010), An ocean-atmosphere climate simulation with an embedded cloud resolving model, *Geophys. Res. Lett.*, *37*, L01702, doi:10.1029/2009GL040822.
Straub, K. H. (2013), MJO initiation in the real-time multivariate MJO index, *J. Clim.*, *26*, 1130–1151.
Straub, K. H., G. N. Kiladis, and P. E. Ciesielski (2006), The role of equatorial waves in the onset of the South China Sea summer monsoon and the demise of El Niño during 1998, *Dyn. Atmos. Oceans*, *42*, 216–238.
Thayer-Calder, K., and D. A. Randall (2009), The role of convective moistening in the Madden–Julian oscillation, *J. Atmos. Sci.*, *66*, 3297–3312.

Tokioka, T., K. Yamazaki, A. Kitoh, and T. Ose (1988), The equatorial 30–60 day oscillation and the Arakawa-Schubert parameterization, *J. Meteorol. Soc. Jpn.*, *66*, 883–901.

Vitart, F. (2009), Impact of the Madden-Julian oscillation on tropical storms and risk of landfall in the ECMWF forecast system, *Geophys. Res. Lett.*, *36*, L15802, doi:10.1029/2009GL039089.

Vitart, F., and F. Molteni (2010), Simulation of the Madden-Julian oscillation and its teleconnections in the ECMWF forecast system, *Q. J. R. Meteorol. Soc.*, *136*, 842–855.

Vitart, F., S. Woolnough, M. A. Balmaseda, and A. M. Tompkins (2007), Monthly forecast of the Madden–Julian oscillation using a coupled GCM, *Mon. Weather Rev.*, *135*, 2700–2715.

Vitart, F., A. Leroy, and M. C. Wheeler (2010), A comparison of dynamical and statistical predictions of weekly tropical cyclone activity in the southern hemisphere, *Mon. Weather Rev.*, *138*, 3671–3682.

Waliser, D. E., K. M. Lau, W. Stern, and C. Jones (2003), Potential predictability of the Madden–Julian oscillation, *Bull. Am. Meteorol. Soc.*, *84*, 33–50.

Wang, M., et al. (2011), The multi-scale aerosol-climate model PNNL-MMF: Model description and evaluation, *Geosci. Model Dev.*, *4*, 137–168.

Wheeler, M. C., and H. H. Hendon (2004), An all-season real-time multivariate MJO index: Development of an index for monitoring and prediction, *Mon. Weather Rev.*, *132*, 1917–1932.

Xie, S., H.-Y. Ma, J. S. Boyle, S. A. Klein, and Y. Zhang (2012), On the correspondence between short- and long-time-scale systematic errors in CAM4/CAM5 for the year of tropical convection, *J. Clim.*, *25*, 7937–7955.

Yanai, M., S. Esbensen, and J. Chu (1973), Determination of bulk properties of tropical cloud clusters from large-scale heat and moisture budgets, *J. Atmos. 30*, 611–627.

Yoneyama, K., C. Zhang, and C. N. Long (2013), Tracking pulses of the Madden–Julian oscillation, *Bull. Am. Meteorol. Soc.*, *94*, 1871–1891.

Zhang, C. (2005), Madden-Julian oscillation, *Rev. Geophys.*, *43*, RG2003, doi:10.1029/2004RG000158.

Zhang, C. (2013), Madden-Julian oscillation: Bridging weather and climate, *Bull. Am. Meteorol. Soc.*, *94*, 1849–1870.

Zhang, F., N. Bei, R. Rotunno, C. Snyder, and C. C. Epifanio (2007), Mesoscale predictability of moist baroclinic waves: Convection-permitting experiments and multistage error growth dynamics, *J. Atmos. Sci.*, *64*, 3579–3594.

Zhang, G. J., and N. A. Mcfarlane (1995), Sensitivity of climate simulations to the parameterization of cumulus convection in the Canadian climate centre general circulation model, *33*, 407–446.

Zhu, H., H. H. Hendon, and C. Jakob (2009), Convection in a parameterized and superparameterized model and its role in the representation of the MJO, *J. Atmos. Sci.*, *66*, 2796–2811.